


Wall-pressure fluctuations in attached compressible turbulent cavitating flowsChangchang Wang ^{1,2,*}, Guoyu Wang,¹ Mindi Zhang,¹ Biao Huang,¹ and Yi-Qing Ni²¹*School of Mechanical Engineering, Beijing Institute of Technology, Beijing 100081, China*²*Department of Civil and Environmental Engineering, Hong Kong Polytechnic University, Hong Kong 999077, China* (Received 8 January 2022; accepted 19 September 2023; published 6 November 2023)

Unsteady wall-pressure fluctuations are of great interest to gain insight into the structures and physical mechanisms of the turbulence flows that generate the pressure fields. Wall-pressure fluctuations are investigated in high Reynolds number cavitating flows in a wide range of cavitation regimes, with the aim of providing a quantitative understanding of cavitation-induced wall-pressure fluctuations and their scaling behaviors. The experiment is conducted at a high-speed water tunnel with a backward-facing wedge test model, and a simultaneous sampling technique is adopted to synchronize the transient cavity behaviors by high-speed imaging and cavitation-induced wall-pressure fluctuations using four flush-mounted unsteady pressure transducers beneath attached cavities. The results show that with decreasing σ , transient cavity length oscillations increase with cavity regimes changing from a stable inception cavity and an intermittent sheet cavity to an unsteady quasiperiodic cloud cavity, while the time-averaged cavity structures under different cavity regimes present self-similarity. The evolution of mean cavity metrics (i.e., L_c , L_{1c} , t_c , and θ) is examined. Inspired by this geometrical self-similarity, statistics (i.e., root mean square pressure level, probability density function, pressure spectra, convective velocity) of wall-pressure fluctuations both inside and outside the attached cavitation are examined. Specifically, the root mean square value of wall-pressure fluctuations approaches its maximum near the cavity closure, and its amplitude is independent of the cavitation number. The probability density function (PDF) shape presents non-Gaussian and asymmetric behaviors. Generally, the PDF shape is positively skewed at the cavity leading edge, approaching Gaussian behaviors near cavity closure and slightly negatively skewed outside the cavity. Spectral analysis indicates that the scaling regions obtained by fast Fourier transform are usually classified as (1) low-frequency range; (2) mid-frequency range, spectra typically show the f^{-2} behavior; (3) transition range, with a $f^{-7/3}$ relation; and (4) high-frequency range, with a $f^{-3.2}$ relation. Remarkably, the Reynolds number effects significantly enhance the non-Gaussian and asymmetric behaviors of wall-pressure fluctuation PDFs. Our study can help to improve both cavitation modeling and hydraulic designs.

DOI: [10.1103/PhysRevFluids.8.114301](https://doi.org/10.1103/PhysRevFluids.8.114301)**I. INTRODUCTION**

In turbulent cavitating flows, the pressure distribution is of fundamental importance to understand the inception and subsequent development of cavitation [1]. Cavitation generally occurs if the local static pressure drops below the saturated vapor pressure, and consequently, the negative pressures are relieved by forming gas-filled or gas- and vapor-filled cavities [2]. When compared with single-

*Correspondence author: wangchangchang026@vip.163.com

phase liquid or gas flows, a unique feature of the pressure fields in cavitating flows is the existence of a cutoff pressure region (i.e., vapor pressure) where an abrupt dynamic phase change between liquid and vapor phases occurs in response to local pressure fluctuations. In other words, cavity structures are controlled by pressure fields that determine the phase change rate (i.e., evaporation or collapse) and thus cavity growth or collapse. Turbulent cavitation is also responsible for undesirable effects or even damage in hydrodynamic systems, including pumps, turbines, propellers, pipelines, and underwater bodies [3–8], and has recently gained substantial attention. Most of these problems are associated with the pressure fluctuations generated by unsteady cavity behaviors, which are an important source of the corresponding significant vibrations and loud noise in practical applications.

Due to the lack of knowledge of pressure fluctuations, one of the limitations of the current cavitation theory and modeling, especially in sheet/cloud cavitating flows [9,10], is that a uniform saturated vapor pressure is always assumed within the cavitation region, and the local static pressure [11,12] is used to determine the phase change rate. The fluctuating pressure fields in cavitating flows, particularly under sheet/cloud cavitation regimes, have been experimentally shown to be nonuniform and highly unsteady and consist of complex flow structures, e.g., reentrant jets [13] and shockwaves [14]. To understand the dynamics of turbulent cavitating flow, we need to extend our understanding of the pressure fields to include the dynamics of pressure fluctuations.

Many studies have been conducted focusing on the pressure distribution fields in cavitating flows, e.g., the mean static pressure [15–17] and the time evolution of pressure fluctuations associated with transient cavity behaviors. In terms of the pressure fluctuation fields in inception cavitation, by utilizing microscopic bubbles as pressure sensors to measure free-stream pressure fluctuations within turbulent flows far from the solid surface [18–20], the statistics of pressure fluctuations in turbulent cavitating flows and their effects on cavitation inception are investigated [21]. The study showed that a Gaussian distribution slightly skewed toward positive values of fluctuating pressure fields was observed for a 3.17 mm jet [18]. Using this novel technique for determining instantaneous spatial pressure distributions, Liu and Katz [1] experimentally measured the mean and fluctuating pressure distributions under cavitation inception conditions for 2D turbulent shear layer flow past an open cavity. Their study showed that the lock-on behavior of cavitation inception on top of the cavity trailing edge was in agreement with local pressure fluctuations. Furthermore, the periodic elimination of the pressure minimum was found to be due to the flow induced by shear layer vortices passing by the trailing edge of the cavity. Subsequently, Porta *et al.* [22] found that with decreasing hydrostatic pressure, the cavitation activity (low-pressure events) increases exponentially in large-Reynolds-number turbulence flows, indicating the exponential tail of the pressure probability density function (PDF), which provides evidence of intermittency. Motivated by cavitation inception modeling, Bappy *et al.* [23] numerically studied the Lagrangian statistics of pressure fluctuation events (low-pressure fluctuations) in homogeneous isotropic turbulent fields using direct numerical simulation (DNS). Their study showed that the average frequency of low-pressure events has an exponential tail toward very low pressure thresholds, and the PDF of the low-pressure events is heavy-tailed and departs from a totally random homogeneous stochastic process (e.g., Poisson process), indicating a highly intermittent process with a bursty process. Furthermore, the most likely duration between low-pressure events is smaller than the Kolmogorov timescale. Subsequently, Bappy *et al.* [24] investigated pressure statistics along the trajectories of gas nuclei in homogeneous isotropic turbulence at $Re_\lambda = 150$. They found that cavitation inception occurs at mean pressures several kPa above vapor pressure. Moreover, large gas nuclei are found to be more attracted to the vortex cores and spend more time at low-pressure regions than smaller nuclei.

However, such a method cannot be easily extended into the developed cavity, e.g., sheet/cloud cavitation, where the vapor/gas void fraction is much higher. Studies have been conducted to study the temporal features and the correlation with transient cavity behaviors of the wall-pressure fluctuations induced by cavitation on the surface of a solid body [25–28]. Specifically, Le *et al.* [29] experimentally measured distributions of the pressure pulse height spectrum (PPHS) by mounting pressure transducers on a foil surface. Their study indicated that under a thin, well-closed, and stable cavity, pressure pulse distributions exhibit a strong maximum centered at the cavity closure;

under a thicker, open, and unstable cavity, the pressure pulse distribution widens; for a cavity with a periodically shedding cavity cluster, no definite maximum in the pressure pulses was observed. Reisman *et al.* [30] discussed the pressure pulses of large amplitude and short duration caused by the rapid collapse of cloud cavities and identified two different types of pressure pulses, local pulses, and global pulses. By examining synchronized high-speed movies, they observed that the local pulses were associated with a crescent-shaped region of low void fraction and leading-edge structures, while the global pulses were found to be caused by global cloud collapses. These cavitation structures associated with pressure pulses were supposed to be shockwave structures, which have been recently investigated by Ganesh *et al.* [14] using x-ray densitometry. Leroux *et al.* [31] studied unsteadiness in partial cavitation based on wall-pressure measurements on a NACA66(mod) hydrofoil. Periodic pressure fluctuations corresponding to the cavity structure evolution were observed. Their studies showed strong pressure fluctuations at the cavity closure and wake regions where the flow fields recover the noncavitating flow downstream, while within the cavity, the pressure coefficient is constant and approximately the average value between the cavitation number (vapor) and the noncavitating pressure coefficient (liquid), even in periodic cloud cavitation. It should be noted that in the process of cavity cloud collapse, large pressure pulses along with strong pressure fluctuations were captured, which were caused by shockwave generation and propagation. Most recently, Chen *et al.* [32] studied the correlation between pressure fluctuation signals and unsteady cavitation behaviors using a synchronized measurement and observed an increase in pressure fluctuations when cavity closure arrives at the transducer. The propagation speed of pressure pulses in different cavitation regions is found to be related to the bubble density distribution and smaller than the sonic speed in the pure liquid. Ganesh *et al.* [14] experimentally measured the evolution of wall-pressure fluctuation signals when the bubbly shockwave passed by synchronization with high-speed x-ray densitometry on a wedge model. Their measurement successfully captured the pressure rise caused by the bubbly shockwave. Wu *et al.* [27] employed unsteady pressure transducers to study the wall-pressure fluctuations on a NACA0015 hydrofoil. In a study of the physical process of different cavity breakup and shedding mechanisms, namely, the reentrant jet mechanism and shockwave mechanism, Wang *et al.* [33] observed that under the reentrant jet mechanism, relatively lower pressure fluctuations were captured at the head of the reentrant jet, and under the shockwave mechanism, a large pressure pulse was captured at the shockwave front during its propagation. Esposito *et al.* [28] experimentally investigated the spectral and modal features of cavitating flows through an orifice. In their study, multiscale proper orthogonal decomposition (mPOD) was used for high-speed visualizations to extract the dominant spatial and temporal cavitation structures. Wall-pressure fluctuation signals under different cavitation numbers and their dominant frequencies were analyzed. Although the abovementioned studies provided some insights into pressure fluctuations induced by turbulent cavitation flow, e.g., the correlation between pressure pulses and certain cavity structures (e.g., bubbly shockwaves) and pressure fluctuations at cavity closure, there is very limited knowledge on the statistics of wall-pressure fluctuations and their scaling behaviors with cavitation number and Reynolds number, especially in sheet/cloud cavitating flows.

Motivated by the lack of understanding of the statistics of wall-pressure fluctuation fields associated with attached turbulent cavitating flows, especially sheet/cloud cavitating flows, here we report a systematic investigation of wall-pressure fluctuations beneath and downstream of the attached cavitation. A simultaneous sampling technique synchronizing the wall-pressure fluctuation signals and transient cavity behaviors is employed. The present paper is structured as follows: details about the measurement setup and flow conditions are given in Sec. II. The main results are presented in Sec. III, while discussions and concluding remarks are given in Sec. IV.

II. EXPERIMENTAL SETUP

A. Water tunnel and measurement system

The experiments are conducted in a closed-loop recirculating cavitation water tunnel, as shown in Fig. 1, as described in detail by Li *et al.* [34]. The test section of the tunnel has dimensions of

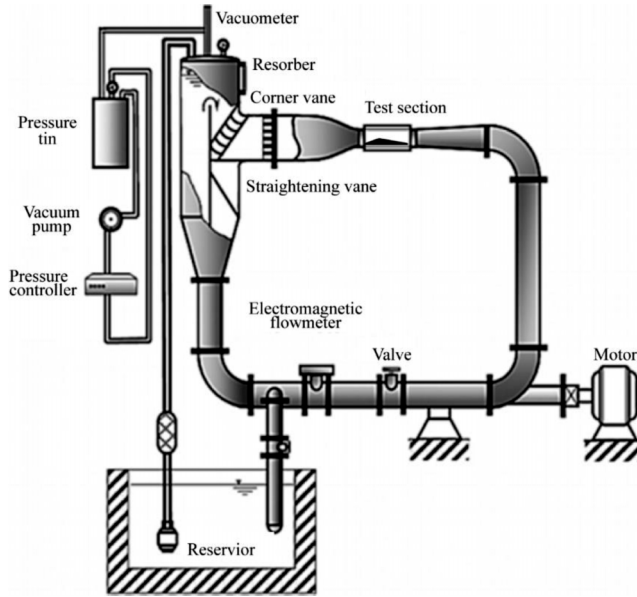


FIG. 1. Schematic of the water tunnel (WT).

700 mm in length and 70 mm \times 190 mm in cross section and has transparent windows at the top and front sides, which are made of Perspex for observations and optical-based measurements. An axial pump located approximately 5 m below the test section is used to drive the flow into the water tunnel to reduce the likelihood of pump cavitation. A tank with a volume of 5 m³ is placed upstream of the test section to separate the undesired free stream bubbles in the flow. To reduce the turbulence level and make the flow uniform, a corner vane and a straightening vane are equipped between the tank and the test section. A vacuum pump connected to the top of the tank is used to control the operating pressure in the tunnel. The upstream pressure and the flow velocity are measured by the vacuumeter (model Y-60, by SALANE, with 0.25% uncertainty) and the electromagnetic flowmeter (product code TDS4033-1CA00-1AA6A01, by Tianjin Kentai, with 0.5% uncertainty), respectively. The highest operating velocity in the tunnel test section is 20 m/s, and the turbulence intensity level is smaller than 2%, except for the near-wall area [34]. Before conducting experiments, the water in the reservoir is kept still for plenty of time to ensure the complete precipitation of the sediment and gas to separate the undesired free stream bubbles in the flow.

In the present study, a backward-facing wedge model (BFWM) is designed to generate cavitation (Fig. 2). As shown in Fig. 2, this wedge is installed on the bottom wall of the 700 mm test section to form a convergent-divergent channel with convergent angle and divergent angle of 20° and 10°, respectively, and the contraction ratio at the throat is 0.5. Cavitation occurs and develops in the divergent section. The throat height of the wedge is $H = 95$ mm, which is half of the test section height, resulting in the length of the convergent channel $L_{\text{convergent}} = 95 / \sin 20^\circ = 278$ mm and the length of the divergent channel $L_{\text{divergent}} = 95 / \sin 10^\circ = 547$ mm. The front view in this flow channel is used to observe a separated-vortex type of cavitation generated from the throat of the convergent-divergent channel. The flow direction is from left to right. The wedge dimensions are maintained to within 1% uncertainty at the angle of the convergent-divergent section. Wall-pressure fluctuations are measured within a region extending from the wedge throat to 16% $L_{\text{divergent}}$. Four PCB piezoelectric transducers (model W102A05, diameter $d = 8.61$ mm, ± 0.014 MPa, sensitivity 7.3 mV/kPa) connected to an ICP Sensor 428C16 signal conditioner are flush mounted with the wall surface in the centerline of the divergent section. The pressure transducers are aligned in the

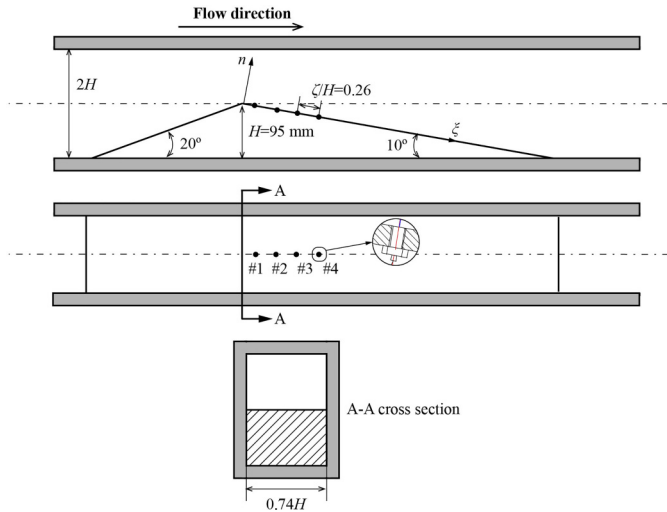


FIG. 2. Schematic of the test section. A backward-facing wedge with four dynamic pressure transducers was installed in the WT test section. ζ is the spacing of the pressure transducers. The (ξ, n) axis system used in this paper is also shown with ξ as the direction along the divergent section surface and n as the direction perpendicular to the divergent section wall surface.

streamwise direction from $\xi/H = 0.11$, with a step of $0.26 H$ (where ξ denotes the streamwise coordinate from the throat along the divergent channel wall surface, as shown in Fig. 2). The locations of the four transducers (ξ/H) are 0.11 for no. 1, 0.37 for no. 2, 0.63 for no. 3, and 0.89 for no. 4. The resonance frequency of the transducers is more than 250 kHz, and the diameter size of the measurement surface is 5.5 mm. The calibration of the sensors is carried out by using the on-site calibrator of PCB Piezotronics, Inc., as the reference. Figure 3 shows the power spectral density (PSD) distribution of the unsteady pressure fluctuations under different flow conditions to test the background noise level. From Fig. 3 it can be found that the intensity of the environmental

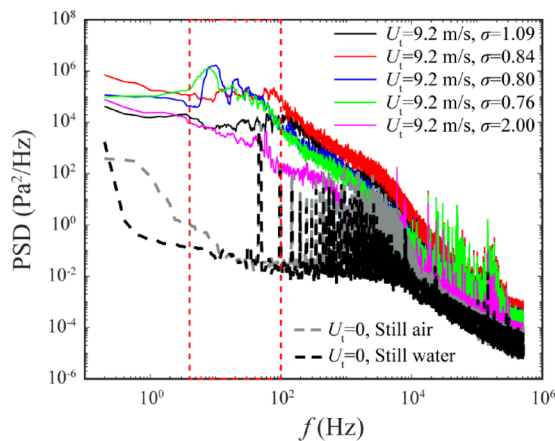


FIG. 3. Power spectral density (PSD) of wall-pressure fluctuations under air and still water, noncavitating flows ($\sigma = 2.00$) and different cavitation conditions ($\sigma = 1.09, 0.84, 0.80$ and 0.76) at a fixed throat velocity $U_t = 9.2 \text{ m/s}$. $\xi/H = 0.63$.

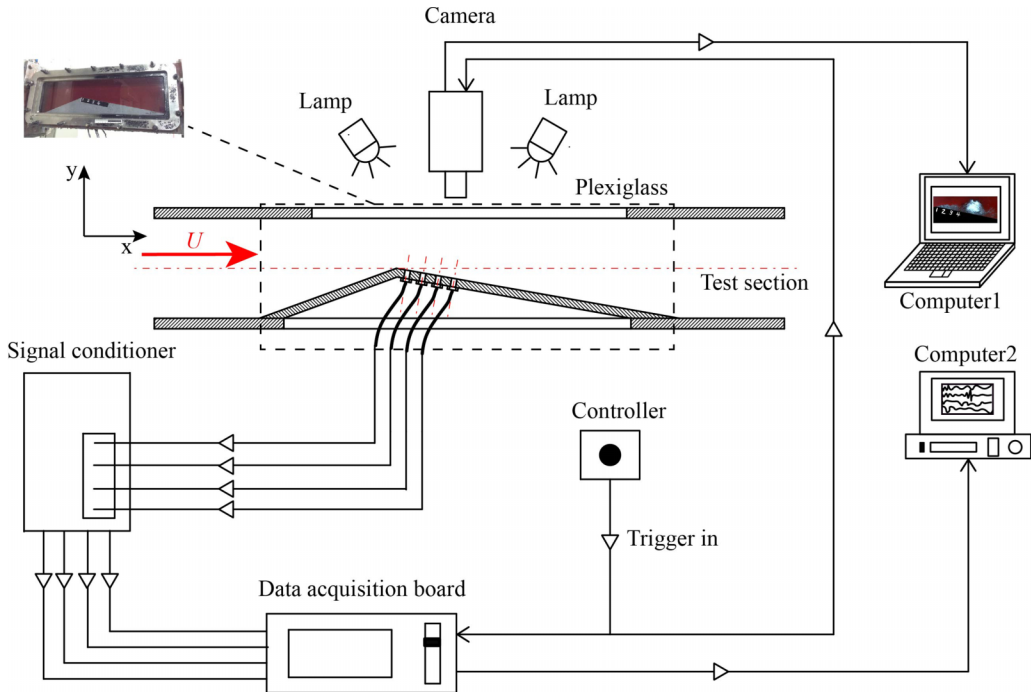


FIG. 4. Schematic of the simultaneous measurement system. The inset image shows the front view of the convergent-divergent channel inside the test section. The (x, y) axis system used in this paper is also shown.

disturbance is small and background noise can be ignored compared to the pressure fluctuations induced by the cavitating flows in the following sections. A 16-bit 16-channel NI DAQ data acquisition system (PCI-6133) with a maximum sampling rate of 2.5 M per channel is used to amplify, filter, and transform the output of transducers into digital values, and depending on the focus of the investigation, 1.024 MHz is used, and the sampling length is 10 s in the present study.

To correlate the pressure fluctuations with the transient cavity behaviors, high-speed imaging and pressure fluctuation signals from four pressure transducers are acquired simultaneously. Figure 4 shows the schematic of the simultaneous sampling system. The synchronization between the high-speed imaging and the pressure transducer measurements is provided by a 5 V TTL signal controller, which is a single-shot waveform generator. When the controller is triggered, the voltage signal will jump to a higher value above the threshold value (20 mV is used in the present work), and the cavitation images and wall-pressure signals will be captured simultaneously at each sampling rate. High-speed imaging in the region downstream of the wedge throat is conducted to visualize the cavity behaviors. A high-speed digital camera (HG-LE, Red Lake) capable of a maximum sampling frequency of 10^5 frames/s is employed to capture the transient cavity structures. The necessary continuous light source is provided by two dysprosium lamps (1 kW). High-speed imaging is recorded at 3000 fps to maintain desirable spatial resolutions depending on the focus of the investigation, and the total data sample size is 1.5 s. Considering that the sampling rate of the high-speed camera (3000 fps) is far less than that of the unsteady pressure transducers (1.024 MHz), which means that three pictures correspond to 1024 pressure samples, the synchronism of the cavitation images and the pressure signal is approximately $3 \mu\text{s}$, and the time delay can be negligible compared with the unsteady sheet/cloud cavitation behaviors, the timescale of which is on the order of approximately 1 ms.

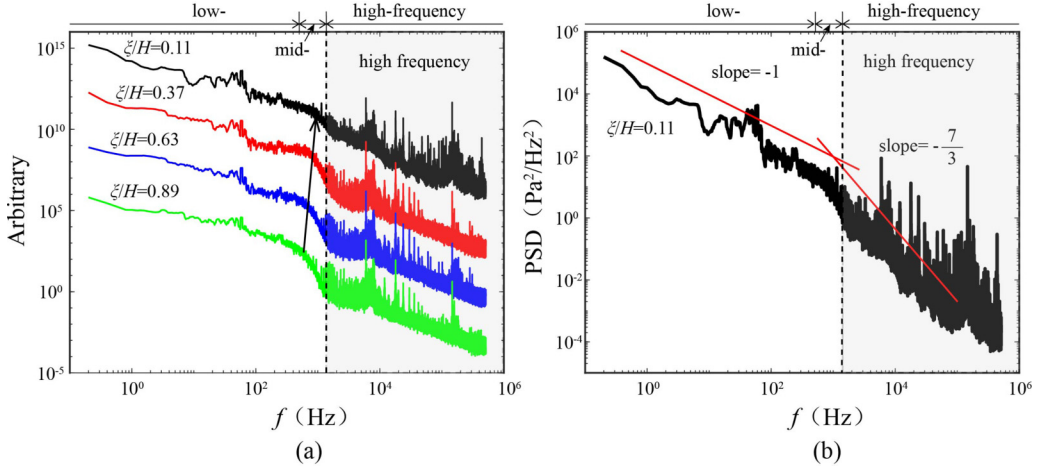


FIG. 5. (a) Power spectral density function (PDF) distribution of wall-pressure fluctuations at pressure transducers 1 through 4 under noncavitating flow conditions ($U_1 = 9.2 \text{ m/s}$, $\sigma = 2.00$) and (b) the scaling behaviors of power spectral density functions on transducer 1. For clarity, the y axis in Fig. 5(a) is shifted.

B. Data processing procedures and uncertainty analysis

1. Wall-pressure fluctuation measurement

The four equidistant unsteady pressure transducers (nos. 1, 2, 3, and 4) provide cavitation-induced wall-pressure fluctuation measurements both inside and outside the mean attached cavity. The raw pressure signals are first preconditioned with a median filter to remove the background noise during the cavitation experiment in the water tunnel. Then, statistical analysis, including the probability density function (PDF), root mean square and other high-order moments (e.g., skewness and kurtosis factors), is conducted. Before the computation of the Fourier spectra, the unsteady pressure signal noise cancellation procedure [35] is conducted, and the wall-pressure fluctuation signals are decontaminated from the background noise measured under the noncavitating flow conditions, which is used as the reference signal in the present study. The contribution of the background noise to the overall spectrum is provided by the coherence function between the measured wall-pressure fluctuation signals under cavitation conditions, $p'_{\text{cav}}(t)$, and the reference wall-pressure fluctuation signals measured under the noncavitation condition, $p'_{\text{non-cav}}(t)$:

$$\gamma_{np}^2 = \frac{|S_{np}(f)|^2}{s_{nn}(f)S_{pp}(f)}, \quad (1)$$

where f is the frequency, S_{nn} and S_{pp} are the autospectra of the pressure fluctuation signals, $p'_{\text{cav}}(t)$ and $p'_{\text{non-cav}}(t)$, respectively, and S_{np} denotes their cross spectrum. The decontaminated pressure signal from the background noise is given as follows:

$$S_{pp}^d = [1 - \gamma_{np}^2(f)]S_{pp}(f). \quad (2)$$

Consequently, the spectra cleaned from the background noise are presented in the following sections. It should be noted that the finite size effects of pressure transducers will significantly influence the unsteady pressure fluctuations, especially their statistics. Figure 5(a) shows the power spectral density function measured by the four unsteady pressure transducers under noncavitating flows. Three frequency regions are clearly revealed, i.e., low- (approximately $< 500 \text{ Hz}$), mid- (approximately $500\text{--}1500 \text{ Hz}$), and high-frequency regions (approximately $> 1500 \text{ Hz}$), where the mid-frequency region serves as the transition between low- and high-frequency regions. It can be observed that approaching the wedge throat, the transition point between the low- and

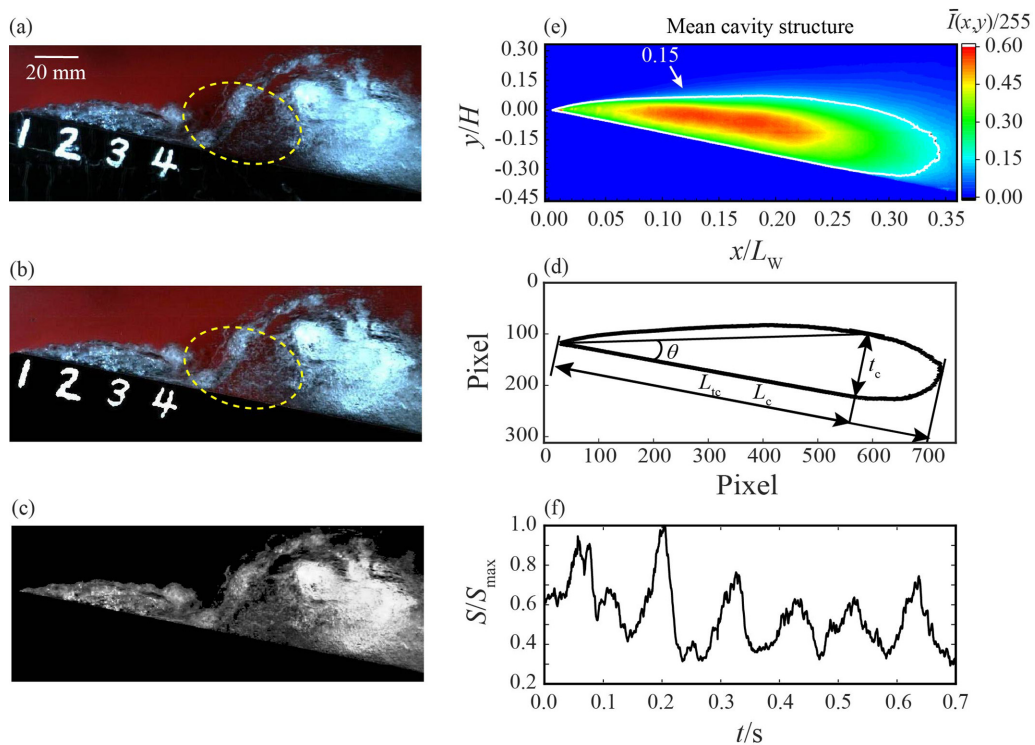


FIG. 6. Typical flow visualization and schematic of the image processing procedure ($\sigma = 0.71$) for (a) raw image, (b) processed image after nonuniform lightness correction, (c) gray image, (d) definitions of cavity geometry metrics, (e) mean cavity topology, and (f) evolution of cavity area during 0.7 s.

mid-frequency regions increases, and the mid-frequency region becomes narrow. As also shown in Fig. 5(b), near the throat at transducer 1, the mid- and high-frequency regions almost merge and follow the $f^{-7/3}$ scaling law. In the low-frequency region, a f^{-1} scaling law can be obtained for all four pressure transducers. Furthermore, a 5.5 mm eddy, which is the same dimension as the transducer effective surface diameter advecting at the lowest U_t in the current experiment, would generate a frequency of approximately 1509 Hz. Thus, frequencies above this value, as shown in the shadow regions in Fig. 5, would experience significant attenuation. The effects of the transducer size would only be relevant at frequencies much larger than the cavitation evolution frequency content, which is in the range of $O(10^1)$ – $O(10^2)$ Hz for the cavitation-induced pressure signal study in our work. Additionally, to avoid this high-frequency attenuation, only the frequency contents between 0 and 1500 Hz are presented in the following sections.

2. High-speed imaging processing

Images are captured at 3000 frames/s at 0.23 megapixels in the front view of the convergent-divergent section with an optical magnification of 0.27 mm/pixel. The image resolution is 752×312 , and the image depth is 8 bit. For all series of images obtained by the visualization method, camera settings for brightness and contrast are kept constant and equal. A schematic of the image processing procedure is shown in Fig. 6. First, the nonuniform lightness in the raw color image [Fig. 6(a)] is corrected using the 2D-gamma function, and the model part is cleaned. As shown in Fig. 6(b), the shadow region as marked by the yellow dashed circle is clearer than that in the raw image in Fig. 6(a). Then, in Fig. 6(c), the cavitation images are converted from RGB true color images to gray images for the convenience of image analysis. In the gray images, each pixel of

an image at location (x, y) has an intensity level $I(x, y)$ ranging between 0 and 255, with 0 for black pixels and 255 for white pixels. By subtracting the background image, the cavitation region is extracted from the wall/vapor region. Quantitative information, including the cavitation area and mean cavity geometric metrics, can be obtained, as shown in Figs. 6(d)–6(f). The normalized gray level is used in the analysis:

$$g(x, y) = I(x, y)/255. \quad (3)$$

The time-averaged gray level is

$$\bar{g}(x, y) = \frac{1}{N_{\text{frame}}} \sum_{N_{\text{frame}}=1}^{N_{\text{frame}}} g(x, y), \quad (4)$$

where N_{frame} is the number of images, and the total images over 1.5 s are used to ensure statistical convergence, which consists of at least 15 cavity shedding cycles. The cavity area is computed based on gray-level weighted pixel statistics as follows:

$$S_{\text{Gray}} = \sum_{x=1}^n \sum_{y=1}^m g(x, y), \quad (5)$$

where n and m are the number of pixels in the horizontal and vertical directions of the cavitation images, respectively. To quantitatively analyze the cavity dimensions, cavity geometric metrics are defined, including the mean cavity length (L_c), mean cavity length at maximum cavity thickness (L_{tc}), maximum mean cavity thickness (t_c), and cavity slenderness factor [θ , $\theta = \arctan(t_c/L_{tc})$], as shown in Fig. 6(d). θ shows the interaction intensity between the cavity and the shear layer across the cavity interface and the cavity region expansion direction. Specifically, a larger θ means that the cavity expands in the vertical direction and a smaller θ in the streamwise direction. The time series of normalized cavity area during 0.7 s in the cloud cavitation regime is presented in Fig. 6(f), showing the periodicity of cavity evolution and the variability from cycle to cycle.

It is worth noting that 3D effects could cause overlapping of different cavity flow structures on cavitation images, altering the intensity distribution, and bring difficulties for the correlation between cavity structures and wall-pressure fluctuation signals. However, in the current study, we focus on the statistical features of both cavity structures and the associated wall-pressure fluctuations. Furthermore, these intensity uncertainties caused by 3D effects can be ignored when compared with the intensity evolution by the transient cavity structure evolution in cavity cycles and the mean cavity structures as well. Consequently, the current visualization and image analysis techniques and the correlation with the associated wall-pressure fluctuation signals are satisfactory for our current study. The velocity at the inlet of the test section is fixed at $U_0 = 4.14, 4.60, 5.03, 5.58, \text{ and } 6.05 \text{ m s}^{-1}$, with an uncertainty of $\pm 0.1 \text{ m s}^{-1}$. The pressure upstream of the test section inlet is varied between $24.5 < p_\infty < 72.5 \text{ kPa}$ with an uncertainty of $\pm 2 \text{ kPa}$. The Reynolds number, $\text{Re} = (U_t H / \nu)$, and cavitation number, $\sigma = (p_\infty - p_v) / 0.5 \rho_l U_t^2$, where U_t corresponds to the velocity at the throat, ν is the water kinematic viscosity, p_∞ is the static pressure at the test section inlet, p_v is the water vapor pressure, and ρ is the water density, are defined. The current Reynolds numbers in the experiments are $\text{Re} = 7.8 \times 10^5, 8.7 \times 10^5, 9.5 \times 10^5, 1.05 \times 10^6, \text{ and } 1.15 \times 10^6$. The cavitation number can be controlled to within 5% uncertainty. The σ was varied from 0.69 to 1.16. Wall-pressure fluctuations in turbulent cavitating flows under different cavitation numbers with five fixed Reynolds numbers are examined in the present study.

III. RESULTS

A. The cavity dimensions

There are a variety of typical cavity flow regimes observed in our experiments, with the sheet cavity regime characterized by small-scale cavity cluster shedding being dominant. In general, there are four distinct cavitation states of cavitating flows (Fig. 7), which include three cavitation regimes

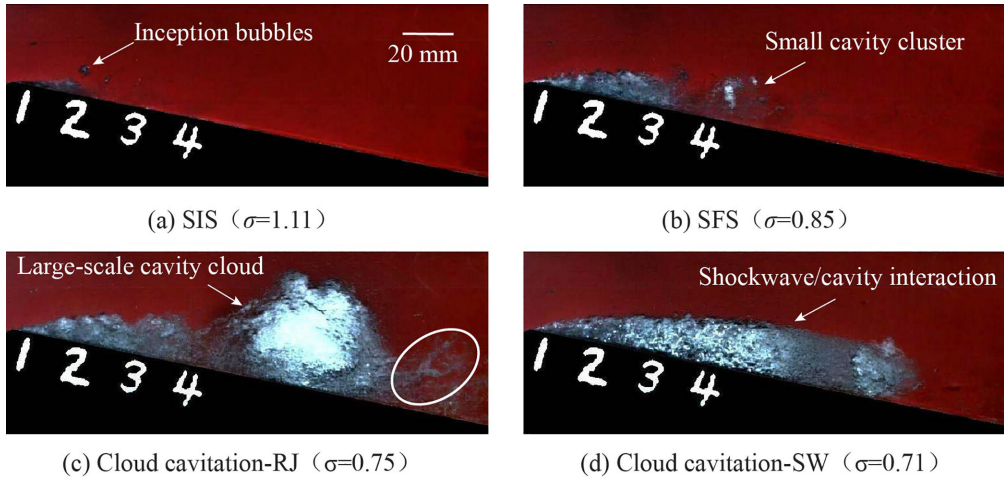


FIG. 7. Four typical cavity behaviors under different cavity regimes: (a) SIS, (b) SFS, (c) cloud cavitation-RJ, and (d) cloud cavitation-SW. $Re = 7.8 \times 10^5$.

(i.e., inception cavitation, sheet cavitation, and cloud cavitation). At first ($\sigma = 1.11$), a stable sheet cavity grows downstream of the wedge throat with separated traveling cavitation bubbles outside the sheet cavity, as shown in Fig. 7(a). Two distinct flow regions can be observed, namely, the shear layer region along the cavity/liquid interface, which is characterized by intermittent generation and collapse of separated traveling cavity bubbles, and the attached cavitation region. This cavity regime is called sheet cavitation with an inception shear layer (SIS). It should be noted that the transient sheet cavity length (L_{ct}) attached to the wall is relatively stable, and no significant cavity cluster shedding from the sheet cavity is observed, which means that the sheet cavity under this regime is closed and in an equilibrium state. As the cavitation number decreases, the cavity grows with increasing attached sheet cavity length, and the shear layer cavitates considerably, changing from separated trailing bubbles to fully cavitating cavity structures. At $\sigma = 0.85$, these cavity structures in the shear layer eventually merge with the sheet cavity attached on the wall, as shown in Fig. 7(b), which is called sheet cavitation with a fully developed shear layer (SFS). With the shear layer strongly cavitating, the cavity closure becomes unstable where the cavity length experiences small fluctuations, and the small-scale cavity cluster is shed intermittently, as indicated by the white arrow in Fig. 7(b). As the cavitation number is further decreased, at $\sigma = 0.75$ (cloud cavitation-RJ), the cavity length oscillations increase considerably with periodic growth and breakup, and the cavity becomes unstable. Two unstable cloud cavitation regimes are discovered in our experiments, i.e., cloud cavitation with a reentrant jet mechanism (cloud-RJ) and cloud cavitation with a shockwave (cloud-SW). As shown in Fig. 7(c), the periodic formation and shedding phenomenon of a large-scale cavity cloud is observed. This large-scale cavity cloud shedding process is supposed to be caused by the reentrant jet dynamics beneath the cavity, which is called cloud cavitation with reentrant jet dominant cloud shedding (RJ). Due to its destructive features, cloud cavitation has attracted much interest and has been widely documented [9,27,36–39]. Abundant vortex structures are generated around the cavity cloud, as indicated by the white circle in Fig. 7(c), indicating the complex cavitation-vortex interaction in the cloud shedding process. In addition, with a further reduction in the cavitation number to $\sigma = 0.71$, in addition to the large cavity length oscillations with periodic sheet cavity growth and breakup, an upstream propagating flow structure with a low void fraction is captured by the current high-speed imaging within the attached sheet cavitation region, as illustrated by the white arrow in Fig. 7(d). The propagation front collapses the local water vapor, causing the low void fraction behind it. Note that this propagation front (i.e., shockwave front) is also reported by Ganesh *et al.* [14] using x-ray densitometry. When it arrives at the cavity

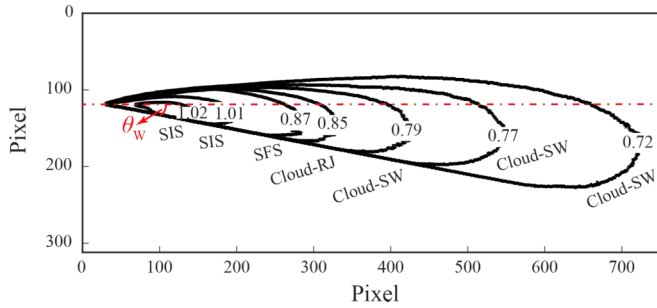


FIG. 8. Evolution of the cavity shapes as a function of σ covering the cavity regimes of SIS, SFS, cloud cavitation-RJ, and cloud cavitation-SW. $Re = 7.8 \times 10^5$.

leading edge at the wedge throat, the attached sheet cavity breaks up, and a large-scale cavity cloud begins to form. This cloud cavitation breakup and shedding mechanism, which is different from the classical reentrant jet mechanism, is called the shockwave-dominated mechanism (SW).

To provide a qualitative view of the cavity dimensions and their variations, the mean cavity shape by varying the parameters Re and σ is extracted and investigated first, as illustrated in Fig. 8. We find that independent of the transient cavity behaviors under different cavity regimes observed in Fig. 7, the mean cavity shape presents the same slender shape. To quantitatively analyze the cavity dimensions, several cavity metrics, including L_c (mean cavity length), L_{tc} (mean cavity length corresponding to the maximum cavity thickness), t_c (maximum mean cavity thickness), and θ (mean cavity slenderness factor), are defined and presented in Fig. 9 as a function of σ at Reynolds numbers of $Re = 7.8 \times 10^5$, 8.7×10^5 , 9.5×10^5 , 1.05×10^6 , and 1.15×10^6 , respectively, and the corresponding fitting curves are also shown. In Fig. 9 different cavity regimes (i.e., inception cavity, sheet cavity, and cloud cavity) are indicated by shadow regions. Here, considering the unsteadiness at cavity closure, which causes cavity length oscillations, especially in sheet cavities and cloud cavities, the mean cavity dimensions were used as cavity metrics. There is no observable Re number dependence on either the mean cavity length or thickness.

As shown in Fig. 9, for the mean cavity length L_c , as σ decreases, the normalized mean cavity length L_c/L_w increases exponentially and is almost proportional to $\sigma^{-4.854}$. Furthermore, with increasing Re , L_c/L_w collapses well to a curve, indicating that the mean cavity length is independent of the Re effects across the range of Re studied. A similar trend has been found in maximum mean cavity thickness t_c and mean cavity length at maximum cavity length L_{tc} , where L_{tc}/L_w is proportional to $\sigma^{-5.152}$ and t_c/L_w is proportional to $\sigma^{-3.829}$. Generally, mean cavity dimensions, including L_c , L_{tc} , and t_c , increase as σ decreases with a negative exponential relation, which has also been observed by Laberteaux and Ceccio [13] and Ganesh *et al.* [14]. This negative exponential relation of mean cavity dimension growth with σ indicates that at higher σ values (i.e., inception and sheet cavity), mean cavity dimensions change slowly, while at lower σ values (i.e., cloud cavity), a small variation in σ could cause large variances in the mean cavity dimensions, showing strong flow instabilities in cloud cavitating flows. The collapse of mean cavity dimensions, especially the mean cavity length in Re , has also been reported by previous studies on hydrofoils [9,18,39] and venturi [9], and the large variation in cavity length at small σ is attributed to the small pressure gradient in the rear part of the cavity [17]. Remarkably, for the mean cavity slenderness factor (θ), in general, with the decrease in σ , θ first increases and then decreases, as shown in Fig. 9(d), while no obvious collapse between different Re values is observed. Based on the definition of θ , as shown in the schematic in Fig. 9(d), a larger value of cavity slenderness factor θ means that the cavity expands mainly in the vertical direction and thus cavity/liquid impingement in the vertical direction, and a smaller value of θ means that the cavity expands mainly in the streamwise direction and thus cavity/liquid impingement in the streamwise direction. Generally, for a fixed σ , θ under

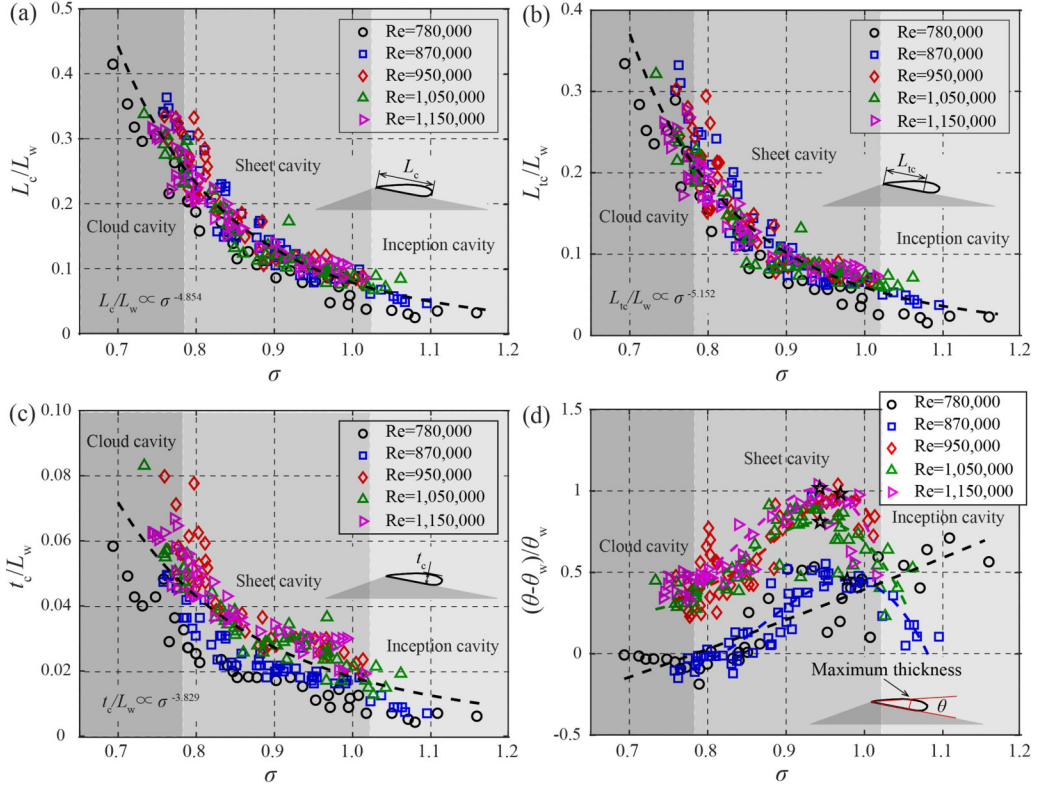


FIG. 9. Variation of (a) average cavity length, L_c/L_w , (b) average cavity length at maximum cavity thickness, $L_{t,c}/L_w$, (c) maximum mean cavity thickness, t_c/L_w , and (d) dimensionless cavity slenderness factor, $(\theta - \theta_w)/\theta_w$, with σ for five Reynolds numbers. Dashed lines show the fitting trend lines of each parameter. L_w is the length along the wall surface of the divergent section channel, and θ_w is the divergent angle. See inset sketches for the definition of cavity dimensions.

low Re conditions ($Re = 7.8 \times 10^5$ and 8.7×10^5) is smaller than that under high Re conditions ($Re = 9.5 \times 10^5$, 1.05×10^6 , and 1.15×10^6). Additionally, except for $Re = 7.8 \times 10^5$, where θ decreases monotonically with decreasing σ , θ experiences an increase and then decreases with the maximum values marked by asterisks for $Re = 8.7 \times 10^5$, 9.5×10^5 , 1.05×10^6 , and 1.15×10^6 . A larger value of θ at high Reynolds number conditions indicates that the Reynolds number effects significantly influence the flow characteristics of cavity interface at maximum cavity thickness, and thus the interactions between cavity interface and bulk flows. As shown in Fig. 9(d), the maximum θ falls in the sheet cavity regime, where at inception cavitation and sheet cavitation at larger σ , θ increases with decreasing σ , while at sheet cavitation at smaller σ and cloud cavitation, θ decreases with decreasing σ . Based on the observations in high speed imaging in Fig. 7, the increase in θ with decreasing σ at sheet cavity regime could be due to the small-scale shedding cavity clusters at the rear of attached sheet cavity and thus the cavity expands mainly in the vertical direction; while the decrease in θ with decreasing σ at sheet cavitation at smaller σ and cloud cavitation is due to the large-scale shedding cavity cloud downstream, and thus the cavity expands mainly in the streamwise direction. Furthermore, to quantitatively characterize the location of cavity interface at maximum cavity thickness, we define a normalized parameter $(\theta - \theta_w)/\theta_w$, where $\theta_w = 10^\circ$ is the divergent angle of the divergent section, which represents the relative location of cavity interface at maximum cavity thickness to the center line of the divergent section as indicated in

Fig. 8. It is worth noting that the single phase flows behind the convergent-divergent channel are characterized by a separated shear layer, a recirculation region, and a reattachment region, where the shear layer, starting from the separation point at the throat, is usually along the center line of the divergent section, and the recirculation region is beneath the shear layer and confined by the wall. As a consequence, θ_w could also represent the location of shear layer in single phase flows and $(\theta - \theta_w)/\theta_w$ represents the relative location between cavity interface and shear layer in single phase flows. When $(\theta - \theta_w)/\theta_w > 0$, the cavity interface at the maximum cavity thickness is above the test section center line, indicating that the cavity interface is located above the shear layer in single phase flows and strong interactions between cavity interface and shear layer in single phase flows; when $(\theta - \theta_w)/\theta_w < 0$ at an early stage of cavitation such as cavitation inception in Fig. 7(a), the cavity interface at the maximum cavity thickness is below the center line, indicating that the cavity interface is located below the shear layer in single phase flows and strong interactions between cavity interface and the recirculation region in single phase flows. In cavitating flows, relatively low and even reverse velocity exists in cavitation region near the wall surface and high bulk velocity outside the cavity, and consequently, there exists a cavitation shear layer which is the result of the interactions among cavitation region, shear layer in single phase flows, and bulk flows. In single phase separated and reattached flows, the study by Devenport and Sutton [40] has reported that instabilities in the shear layer are an important source for the wall-pressure signals. Although the quantitative measurements of cavitation shear layer are challenging and inaccessible to the current combined high-speed imaging and wall-pressure fluctuations measurement technique, our normalized parameter $(\theta - \theta_w)/\theta_w$ which indicates the cavity/liquid impingement inside the cavitation shear layer that is significant for understanding the cavity dynamics, could provide information about the characteristics of cavity interface at maximum cavity thickness inside cavitation shear layer. Further synchronized examinations of wall-pressure fluctuations beneath the attached cavity and $(\theta - \theta_w)/\theta_w$ could be conducted in the future to gain more insights into cavity interface at maximum cavity thickness. In the current study, the flow structures and their variation with cavity regimes across the cavity interface are not examined due to the limitations of high-speed imaging, and more details about the flow structures (e.g., in the process of the interactions between the cavity interface and bulk flows, cavity/liquid impingement) could be obtained by x-ray densitometry under well-defined flow conditions and specific scales and high-fidelity numerical simulation tools, e.g., large-eddy simulation (LES).

The cavity metrics used in the current work are based on the mean cavity structures from gray-level intensity by high-speed imaging. As shown in Fig. 7, for the inception cavity where the transient cavity length (L_{ct}) is relatively stable, the flow structures in the closure of the mean cavity length (L_c) are consistent with those in the closure of the transient cavity length (L_{ct}), and we have $L_c = L_{ct}$. For the sheet cavity and cloud cavity, L_c shows significant differences from L_{ct} . For the sheet cavity, owing to the intermittent shedding of the small-scale cavity cluster, there exist L_{ct} fluctuations, and with decreasing σ , the fluctuations of L_{ct} increase considerably, and we have $L_c \approx L_{ct}$. The closure region of L_c is mainly influenced by both the closure of the transient sheet cavity and the small-scale shedding cavity cluster. For cloud cavities, cavity structures are characterized by periodic leading-edge breakup and large-scale cavity cloud shedding and are influenced by the shedding cavity cloud. The mean cavity length is larger than the transient maximum sheet cavity length, and we have $L_c > L_{ct}$. In addition, the flow structures are affected periodically by the process of sheet cavity growth and large-scale cavity cloud shedding. The differences between L_c and L_{ct} , which are important for understanding the physics (e.g., statistics) involved in cavitating flows, are investigated in the following.

To elucidate the periodicity in the cloud cavitation regime, the variation in the Strouhal number ($St = fL_c/U_t$) based on L_c and U_t upon a change in Re is examined using both the measured pressure signals and cavity area obtained from cavitation images. The dominant shedding frequency f is calculated from both the cavity area evolution obtained from the imaging processing procedure in Fig. 6 and pressure fluctuation signals. Figure 10 shows the variation in mean St as a function of Re along with the data in venturis collected from the published literature and the corresponding fitting

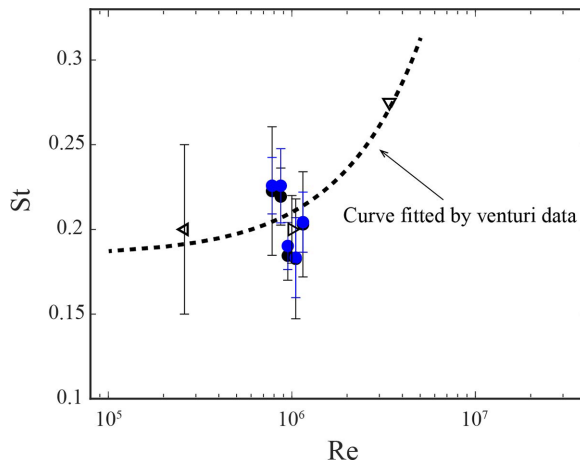


FIG. 10. Comparisons of the variation in St in cloud cavitation based on L_c and U_t measured in the present experiments from both pressure signals and cavitation images and the data in the literature as a function of Re . ∇ , Lush and Peter [41]; \triangleright , Stutz *et al.* [42]; \triangleleft , Dular *et al.* [43]; \bullet , present, pressure signals; and \bullet , present, image. The pressure transducer location is at $\xi/L_c = 0.63$. The standard deviation is calculated using St for at least five cavitation numbers at a fixed Re .

curve. The error bars represent the standard deviation of St in different cloud cavitation conditions at a fixed Re . The current measurements of pressure signals and images show good agreement, and all the current measurement data points fall around the fitted curve. St is approximately 0.2 in the current Re range, which is similar to that reported in the literature.

B. Root mean square of wall-pressure fluctuations

To analyze the statistics of wall-pressure fluctuations, the root mean square pressure coefficient, Cp_{rms} , is defined as

$$Cp_{rms} = \frac{\sigma_p}{0.5\rho U_t^2}, \quad (6)$$

where σ_p denotes the standard deviation of the pressure fluctuations.

From Figs. 8 and 9, it is observed that the mean cavity shape under different cavity regimes that have different cavity lengths L_c presents geometric self-similarity. Consequently, to study the general statistical characteristics of flow fields inside and outside the mean cavity in cavitating flows, e.g., the wall-pressure fluctuation fields, under different cavity regimes, we introduce the nondimensional parameter ξ/L_c to identify the locations in cavitating flows. Here ξ is the distance from the cavity leading edge, and L_c is the cavity length; thus, the nondimensionalized parameter ξ/L_c is defined. When $\xi/L_c < 1$, it is inside the cavity, while $\xi/L_c > 1$, it is outside the cavity at cavity wakes. With the increase in ξ/L_c , the monitor location moves far away from the cavity leading edge. It should be noted that in the current experiment, we have four unsteady pressure transducers; thus, at each cavitation number condition, we have four values of Cp_{rms} , which correspond to four values of ξ/L_c indicating different locations in the cavitating flow fields. By combining all the experimental conditions, we can obtain the general distribution of statistical features of wall-pressure fluctuations both inside and outside the cavity from the statistical viewpoint which are independent on cavity regimes in cavitating flow fields.

The evolution of Cp_{rms} as a function of ξ/L_c under different Reynolds numbers is reported in Fig. 11. With the increase in ξ/L_c , the Cp_{rms} values first increase at $\xi/L_c < 1$ and approach their maximum at $\xi/L_c = 1$ close to cavity closure and then begin to decrease at $\xi/L_c > 1$ downstream of

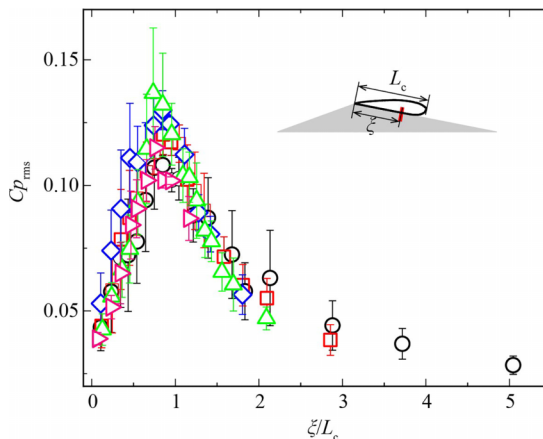


FIG. 11. Distribution of the $C_{p_{rms}}$ in terms of ξ/L_c under different Re, \circ^* , $Re = 7.8 \times 10^5$; \square , 8.7×10^5 ; \diamond , 9.5×10^5 ; \triangle , 1.05×10^6 ; and \blacktriangleright , 1.15×10^6 . The data points from all four pressure transducers under different cavity regimes are collected together, and their means and standard values (error bars) are calculated approximately every $0.1 \xi/L_c$.

cavity closure. Moreover, the wall-pressure fluctuation intensity level attenuation rate downstream of the attached cavitation is far lower than the strengthening rate inside the attached cavitation. It should be noted that similar maximum pressure fluctuations (i.e., peak value) near cavity closure have been also reported for certain stable cavity regimes. Specifically, *Le et al.* [29] reported a strong pressure pulse height spectrum (PPHS) maximum centered at cavity closure under a thin, well-closed, and stable cavity. *Leroux et al.* [31] captured the maximum wall-pressure fluctuation intensity at cavity closure under a stable sheet cavity regime. In the current study, by scaling with L_c , our study shows that this maximum wall-pressure fluctuation intensity near cavity closure is independent of the cavity regimes, even under highly unsteady cloud cavitation regimes. Moreover, the wall-pressure fluctuation intensity is independent of σ as long as it is scaled by the mean cavity length L_c . As shown in Fig. 11, the current results under different Re conditions collapse well both inside and outside the attached cavitation, showing that the phenomenon of $C_{p_{rms}}$ peak at mean cavity closure is independent on Reynolds number effects. However, we do observe the variability of $C_{p_{rms}}$ under different Reynolds numbers even in the limited range of Re studied, e.g., the magnitude of $C_{p_{rms}}$ at $Re = 1.05 \times 10^6$ is higher than that at $Re = 1.15 \times 10^6$. In our work we mainly examine the statistics of wall-pressure fluctuation signals inside and outside the mean cavity and work on the statistics that are independent on cavity regimes. Considering the limited range of Reynolds numbers in our experiment, the Re effects on magnitude of $C_{p_{rms}}$ could be studied with further experiment work in the future. It is noteworthy that this peak phenomenon of maximum wall-pressure fluctuation intensity level near cavity closure is also found to be in accord with that in the single phase separated/reattachment flow where maximum amplitude of the $C_{p_{rms}}$ coefficient occurs at the location of the mean reattachment point of the recirculation bubble [44]. In single phase flow, this absolute amplitude at the reattachment point of the recirculation bubble is independent of Re. In cavitating flows, the evolution of $C_{p_{rms}}$ as a function of ξ/L_c under different Reynolds numbers shows the similar trend. However, we indeed observed the large variability of $C_{p_{rms}}$ at the mean cavity closure region under different Reynolds numbers, and thus the Re effects could be important in cavitating flows. Some other factors such as the uncertainties involved in the measurements, operations, and environments could also attribute to this variability. Further effort could be conducted to examine the $C_{p_{rms}}$ at the mean cavity closure region and the associated Re effects. Furthermore, at the same ξ/L_c , although the cavity geometry and pressure fluctuation

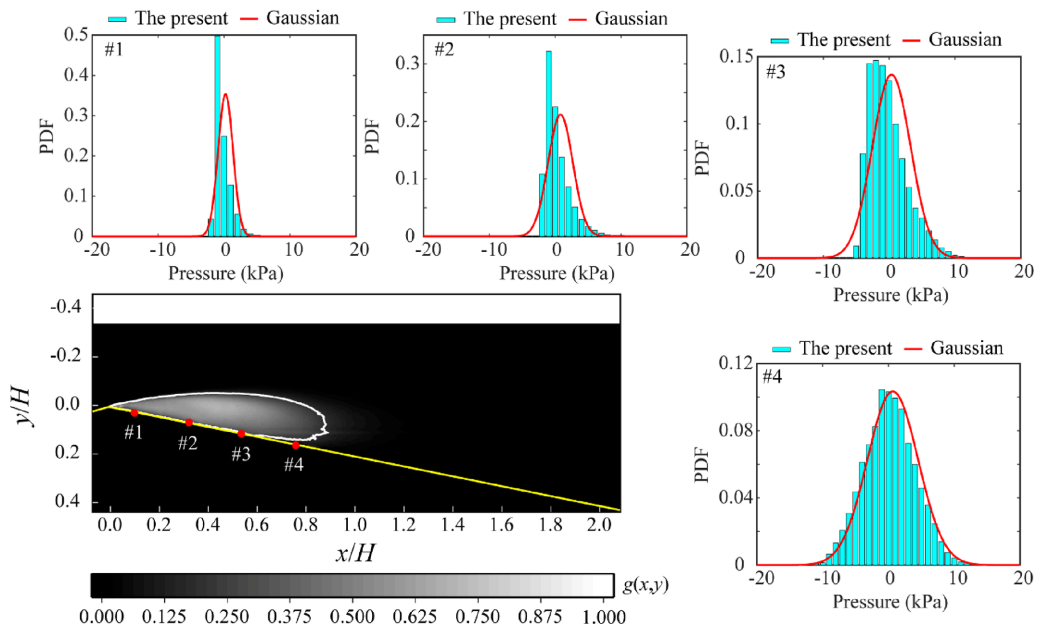


FIG. 12. Probability density functions (PDFs) of wall-pressure fluctuations at different locations ($\xi/L_c = 0.11, 0.39, 0.67, 0.94$) from the cavity leading edge to cavity closure under $Re = 7.8 \times 10^5$ and $\sigma = 0.85$. The red lines show the Gaussian distribution. The inserted pictures show the time-averaged cavity topology.

coefficient could be the same, the cavitating materials under high Re conditions have larger potential damage due to the higher absolute wall-pressure fluctuation intensity.

C. Probability density function of wall-pressure fluctuations

In Fig. 12 the probability density functions (PDFs) are shown at several locations inside the mean attached cavity at $Re = 7.8 \times 10^5$ and $\sigma = 0.85$ for the sheet cavity regime. Under this condition, these four pressure transducers are located uniformly from the cavity leading edge to cavity closure. The PDFs present non-Gaussian nonsymmetric behaviors. Specifically, near the cavity leading edge, the PDFs present positively skewed behaviors, and near the cavity closure, the PDFs approach Gaussian behaviors.

To further analyze the characteristics of wall-pressure fluctuation PDFs, PDFs of wall-pressure fluctuations normalized to the corresponding RMS values were calculated. Figure 13 shows the distributions of the PDF shape of wall-pressure fluctuations inside the attached cavitation as a function of ξ/L_c at $Re = 7.8 \times 10^5$ and $Re = 9.5 \times 10^5$. The data sets used in Figs. 13(a) and 13(b) cover a wide range of cavity regimes, including relatively stable sheet cavitation and unsteady cloud cavitation, and are listed in Table I. As presented in both Figs. 13(a) and 13(b), the PDFs of wall-pressure fluctuations present asymmetric characteristics, and both the positive tails and negative tails deviate from the Gaussian curves considerably, indicating the non-Gaussian distribution of wall-pressure fluctuations inside the attached cavitation. Specifically, the PDFs of wall-pressure fluctuations are dependent on ξ/L_c and positively skewed near the cavity leading edge. From the cavity leading edge to cavity closure, with the increase in ξ/L_c , the long positive tails move toward the Gaussian curve as the deviation from the Gaussian behavior decreases, as indicated by the black arrows in Fig. 13(a). In the same way, the negative long tails also move toward the Gaussian distribution shown in Fig. 13(a). Approaching cavity closure, both the positive long tails and negative long tails almost collapse to the Gaussian curves and show Gaussian behaviors. This dependence on ξ/L_c of the PDF shape shows inhomogeneity inside the attached cavitation. The

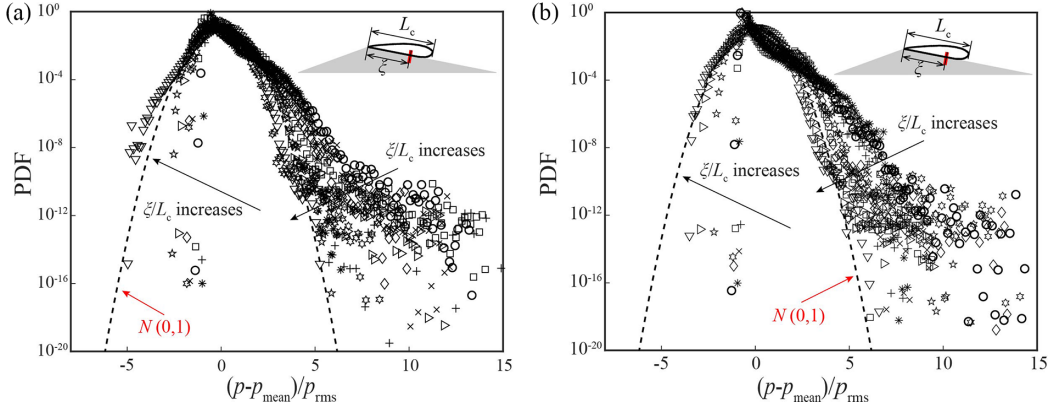


FIG. 13. Distributions of the PDFs of the wall-pressure fluctuations inside the mean attached cavity for (a) $Re = 7.8 \times 10^5$ and (b) $Re = 9.5 \times 10^5$. The experimental conditions are listed in Table I.

long positive and negative tails of the PDFs of wall-pressure fluctuations show that the intermittent behaviors of extreme higher and lower pressure fluctuation magnitude events are nonuniformly distributed inside the mean attached cavity, e.g., large amplitude pressure fluctuations and peaks. Moreover, with increasing Re , this positively skewed feature of the PDF shape is enhanced, as the long positive tails move toward larger pressure fluctuations and the long negative tails move toward smaller pressure fluctuations, as shown in Fig. 13(b). It should be noted that this non-Gaussian behavior for both positive and negative wall fluctuations and its dependence on ξ/L_c and the Reynolds number are also reported by Camussi *et al.* [44] in flows over a forward-facing step, which means that the mean cavity structures resemble the recirculation region in single-phase separated-reattachment flows in terms of the PDF distributions of wall-pressure fluctuations. This resemblance is also found in terms of the distribution of the Cp_{rms} inside the mean attached cavity in Fig. 11.

Figure 14 shows the distributions of the PDF shapes of the wall-pressure fluctuations outside the attached cavitation as a function of ξ/L_c at $Re = 7.8 \times 10^5$ and $Re = 9.5 \times 10^5$. The data sets used in Figs. 14(a) and 14(b) are listed in Table II. As presented in both Figs. 14(a) and 14(b), the PDFs of wall-pressure fluctuations present different features than those inside attached cavitation

TABLE I. Experimental conditions used in Fig. 13.

Marker	$Re = 7.8 \times 10^5$			$Re = 9.5 \times 10^5$		
	ξ/L_c	σ	Cavity regime	ξ/L_c	σ	Cavity regime
○	0.09	0.79	Cloud-RJ	0.10	0.83	Cloud-RJ
+	0.21	0.75	Cloud-RJ	0.21	0.79	Cloud-RJ
*	0.31	0.69	Cloud-RJ	0.31	0.79	Cloud-RJ
×	0.42	0.85	SFS	0.42	0.75	Cloud-SW
□	0.51	0.75	Cloud-RJ	0.52	0.73	Cloud-SW
◇	0.60	0.88	SFS	0.64	0.79	Cloud-RJ
☆	0.72	0.85	SFS	0.74	0.84	SFS
☆	0.80	0.79	Cloud-RJ	0.81	0.80	SFS
▷	0.90	0.79	Cloud-RJ	0.92	0.90	SFS
▽	1.02	0.85	SFS	1.04	0.85	SFS
...	Gaussian distribution			Gaussian distribution		

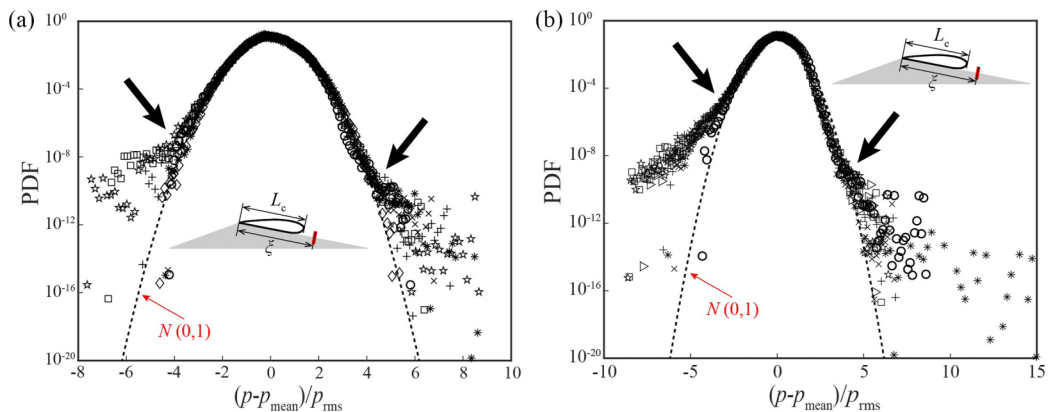


FIG. 14. Distributions of the PDFs of the wall-pressure fluctuations outside the mean attached cavity for (a) $Re = 7.8 \times 10^5$ and (b) $Re = 9.5 \times 10^5$. The experimental conditions are listed in Table II.

in Fig. 13. Non-Gaussian behaviors are observed to be concentrated mainly at the distribution tails. Although asymmetric characteristics where both the positive tails and negative tails deviate from the Gaussian curves are observed, the PDF shape follows a Gaussian distribution well in a wide range of normalized wall-pressure fluctuation values of $-2 < p/p_{rms} < 2$. This feature indicates that outside the attached cavitation at cavity wakes, extremely large (both negative and positive values) wall-pressure fluctuation values present intermittent behaviors, showing the non-Gaussian distribution of wall-pressure fluctuations with large values outside the attached cavitation. Small wall-pressure fluctuation values follow Gaussian behaviors. The PDFs of wall-pressure fluctuations outside the attached cavity are almost independent of ξ/L_c , which is different from that inside the mean attached cavity. Furthermore, as shown in Fig. 14(a), at lower Reynolds number conditions in Fig. 14(a), the negative deviation pressure value of wall-pressure fluctuations that begins to deviate from the Gaussian curve is observed to be approximately $-4p/p_{rms}$, as indicated by the black arrow. The positive deviation pressure value of wall-pressure fluctuations that starts to deviate from the Gaussian curve is approximately $5p/p_{rms}$. The differences between the negative and positive deviation pressure value of wall-pressure fluctuations show the asymmetric behaviors of wall-pressure fluctuation PDFs. Reynolds number effects will significantly influence the deviation pressure values. As shown in Fig. 14(b), with increasing Reynolds number, both the absolute negative critical value and positive critical value of wall-pressure fluctuations decrease, and the range of wall-pressure fluctuation values following a Gaussian distribution becomes narrow. The

TABLE II. Experimental conditions used in Fig. 14.

Marker	$Re = 7.8 \times 10^5$			$Re = 9.5 \times 10^5$		
	ξ/L_c	σ	Cavity regime	ξ/L_c	σ	Cavity regime
○	1.13	0.92	SFS	1.13	0.97	SFS
+	1.40	0.94	SFS	1.30	0.97	SFS
*	1.71	1.08	SIS	1.36	0.90	SFS
×	1.79	1.05	SFS	1.47	0.89	SFS
□	1.87	1.08	SIS	1.62	0.96	SFS
◇	2.12	1.07	SIS	1.75	0.97	SFS
☆	2.45	0.99	SFS	1.89	1.00	SIS
...	Gaussian distribution			Gaussian distribution		

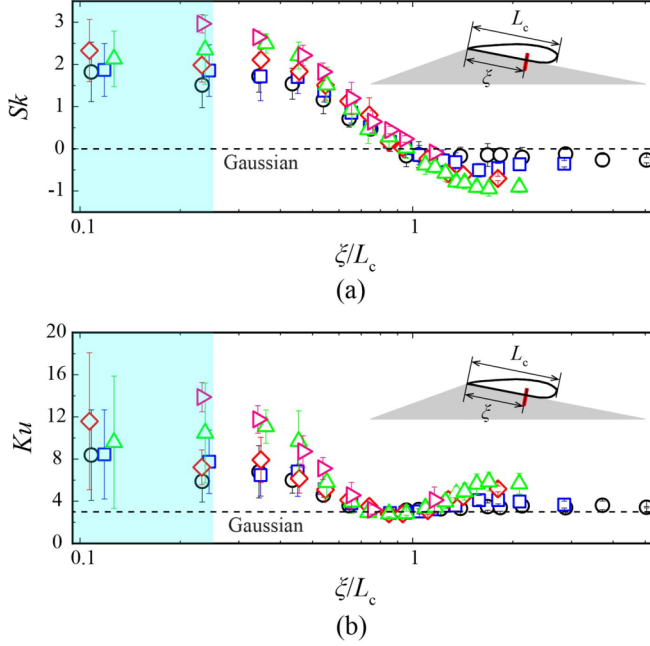


FIG. 15. Evolution of the (a) Sk and (b) Ku values as a function of ξ/L_c under different Re : \circ , $Re = 7.8 \times 10^5$; \square , 8.7×10^5 ; \diamond , 9.5×10^5 ; \triangle , 1.05×10^6 ; and \blacktriangleright , 1.15×10^6 . Dashed lines correspond to the values of a process following the Gaussian distribution. The data points from all four pressure transducers under different cavity regimes are collected together, and their means and standard values (error bars) are calculated approximately every $0.1 \xi/L_c$.

Reynolds number effects on deviation pressure value of wall-pressure fluctuations show that at high Re , the intensity and frequency of local pressure fluctuation extreme events (i.e., negative and positive) increase, leading to a wider range of wall-pressure fluctuation following non-Gaussian behaviors.

To quantitatively analyze the statistics of the wall-pressure fluctuations inside the attached cavitation, e.g., the non-Gaussian and asymmetrical behaviors observed in the PDFs in Fig. 13 and Fig. 14, the high-order moments of wall-pressure fluctuations, including the skewness factor (Sk) and kurtosis factor (Ku), are calculated and presented in Fig. 15. The Sk and Ku of wall-pressure fluctuations are defined as follows:

$$Sk = \langle p'^3 \rangle = \int_{-\infty}^{+\infty} p'^3 P_m(p') dp', \quad (7)$$

$$Ku = \langle p'^4 \rangle = \int_{-\infty}^{+\infty} p'^4 P_m(p') dp', \quad (8)$$

where $P_m(p')$ is the probability density function of wall-pressure fluctuations. Sk presents the asymmetry feature of the PDF of a random variable. For example, asymmetric behavior with a positive Sk shows that events with large positive amplitudes and a negative Sk indicates that events with large negative amplitudes occur frequently. Ku presents the features of the tails of the PDF. A relatively high value of Ku signifies the existence of rare high-amplitude wall-pressure fluctuations associated with the long tails of the PDF. For a Gaussian process, Sk and Ku are 0 and 3, respectively.

As shown in Fig. 15, inside the attached cavitation, high positive Sk values above zero and large Ku values above 3 are observed, indicating non-Gaussian behavior, which is consistent with the observations from the PDF shape in Fig. 13. A strong dependence on ξ/L_c of the wall-pressure

fluctuation PDFs can be observed in Fig. 15. From the cavity leading edge to cavity closure, with the increase in ξ/L_c , both Sk and Ku first show almost constant values, as indicated by the shadow region, and then decrease quickly. Near the cavity closure, the Sk value approaches 0, and the Ku value approaches 3, as indicated by the black dashed lines, which show a Gaussian distribution, showing that in this region, the pressure fluctuations almost follow Gaussian behaviors. Taking the data at $Re = 7.8 \times 10^5$ as an example, from the cavity leading edge to cavity closure, the Sk values change from 3.5 to approximately zero, while the Ku values change from 17.8 to approximately 3. With increasing Re , both Sk and Ku increase, as seen in Fig. 15(b), showing the Reynolds number enhancement effects on this non-Gaussian and asymmetrical behavior of wall-pressure fluctuations. The Re enhancement effects on non-Gaussian behaviors of wall-pressure fluctuations indicates that at higher Re , the frequency of extreme higher pressure fluctuation magnitude events (both negative and positive) increases. Further downstream of the cavity closures shown in Fig. 15, the mean Sk values in this region are slightly negative, and the mean Ku value is slightly larger than 3, indicating that this non-Gaussian behavior still persists in this region and that the negative Sk shows the negative asymmetry features downstream of the cavity closure, which is different from the positive asymmetry features inside the mean attached cavity. Different from that inside the mean attached cavity, first near cavity closure, with increasing ξ/L_c , the absolute values of both Sk and Ku increase, and then at the far fields downstream of the cavity closure, both factors are shown to be almost independent on the distance from the cavity closure. It is worth noting that although cavity behaviors under different cavity regimes (SIS, SFS, RJ, and SW) present distinct cavity patterns based on the observations in Sec. III A: a good collapse of PDFs among different cavity regimes at a fixed Re is observed inside the mean attached cavity in terms of statistical features when scaled by L_c . This shows the self-similarity of flow structures in the mean cavitating flow fields as well, especially the pressure fields, despite different cavity patterns that persist even under unsteady cloud cavitating flows.

D. Hypothesis of physical mechanisms for non-Gaussian behaviors of wall-pressure fluctuations

In the following, to further understand the physical mechanisms of the statistics of wall-pressure fluctuations inside attached cavitation, especially the positively skewed PDF shape, we provide a comparison with the PDF data reported in single-phase flows. It is reported that in incompressible flows, the typical characteristics of pressure PDFs have a negative long tail. For example, in three-dimensional incompressible homogeneous isotropic turbulence flows at $Re_\lambda \leq 60$, Pumir [45] observed an exponential tail on the negative side of the pressure PDF, and the joint PDFs of strain, vorticity, and pressure show a strong asymmetry between positive and negative pressure fluctuations. Additionally, Reynolds number enhancement effects on this exponential behavior are observed. This kind of negative long tail of the pressure fluctuation PDF in high Re turbulent boundary layers at Reynolds numbers based on the momentum thickness $Re_\theta = 20000$ is documented by Tsuji *et al.* [46]. It is worth noting that across the range of Re and σ studied, our transducers captured the pressure signals outside the cavitation region at early stage of cavitation such as cavitation inception and sheet cavitation with larger σ where the cavity length is short and mainly small separated cavitation bubbles exist there. Figure 16 presents the evolution of Sk and Ku outside the cavity as a function of Re_t based on the maximum mean cavity thickness t_c in the current measurements. We find this negative long tail reported in single phase flows [45,46] outside the mean attached cavity in our measurements, which is slightly negatively skewed and independent of the distance from the cavity closure. Due to the limitations of our measurement range of Re and σ , the pressure signals outside cavity under sheet cavity at smaller σ and cloud cavitation with large-scale shedding cloud are not available. Consequently, our current measurement shows that the effects of small separated cavitation bubbles outside the cavitation region at the rear of an inception cavity and sheet cavity at larger σ on the statistics of pressure fluctuations are weak. As shown in Fig. 6, with the increase in Re , Sk becomes negatively smaller and Ku becomes positively larger, showing the Re enhancement effects that is in agreement with the observations by Pumir [45] and

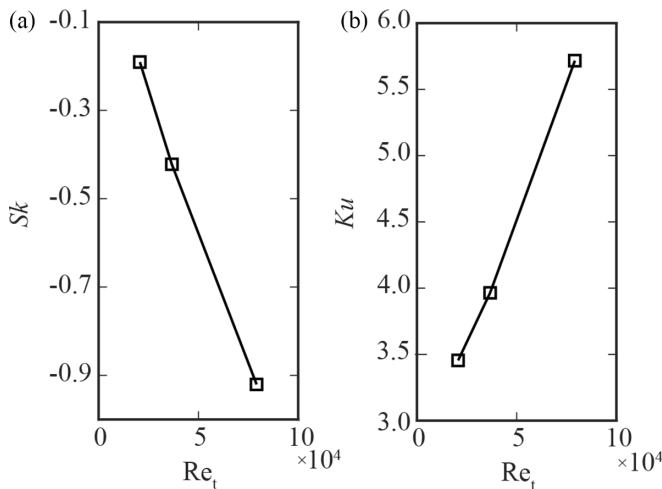


FIG. 16. The evolution of the measured and published values for (a) Sk and (b) Ku values outside the cavity as a function of Re_t . The current measured data are averaged in the far fields downstream of the cavity closure where the high-order moments of the PDF are almost constant, and Re_t is based on t_c .

Tsuji *et al.* [46]. Taking the data at $Re_t = 20681$ ($Re = 7.8 \times 10^5$) based on the corresponding maximum cavity thickness as an example, the mean Sk value in this region in our measurement is approximately -0.20 , and the mean Ku value is 3.42 , and these values are comparable to those in the high Re turbulent boundary layer, which are -0.35 and 4.6 in Tsuji *et al.* [46], respectively.

On the other hand, we find the positively skewed PDF shape inside the cavity and negatively skewed PDF shape near the cavity closure and their dependence on ξ/L_c shown in Fig. 15. As noted in the work by Donzis *et al.* [47], by examining the data sets of compressible flows obtained by direct numerical simulation (DNS) at $Re_\lambda = 43$ – 430 , they found that as the turbulent Mach number increases, pressure fluctuations become stronger, and this asymmetrical negative PDF shape cannot be sustained since pressure fields are a positive quantity and the negative fluctuations are bounded, showing the compressibility effects on the statistics of pressure fluctuations. In cavitating flows, the local sonic speed within cavitating flows is altered by the presence of cavitation bubbles and could be 3 to 5 m/s at vapor fraction around 0.5 in local regions according to the sonic speed formulas [48] and the abrupt phase change will further decrease the sonic speed, resulting in strong compressibility effects in cavitation region compared with that in incompressible single phase liquid flow. Local regions in cavitating flows could even reach sonic and even supersonic state. Consequently, the cavitation compressibility effects could have a significant influence on the statistics of pressure fluctuations in cavitating flows such as the positive skewness and their evolution inside the cavity observed in the current measurements.

The pressure Poisson equation [49] is frequently used to gain insight into the physics of pressure fluctuations. According to classical textbooks [50], two important source terms of pressure fluctuations may be identified in incompressible flow. One is associated with the direct interaction between the gradient of the mean velocity and the gradient of the fluctuating velocity, indicating the flow shear effects on pressure fluctuations. The other reflects the turbulence-turbulence interactions. It is worth noting that in compressible flows, additional source terms involving the mean density gradients will arise. In the present work, we mainly study the effects of shear and compressibility on the statistics of pressure fluctuations and their distributions inside a cavity. The first term shows that the shear effects will directly affect the rapid pressure, which is associated with the positive

large-amplitude pressure fluctuations, and the larger the shear effects are, the more significant the deviation from Gaussian behavior. It is worth noting that strong shear effects occur near the wedge throat (i.e., cavity leading edge) due to the thin cavity thickness shown in Fig. 8 and as the distance from the wedge throat increases, cavity thickness increases and these shear effects weaken till maximum mean cavity thickness, and then gradually decreases due to the decreasing cavity thickness till cavity closure. Considering that the cavity thickness at cavity closure is much larger than that at cavity leading edge, the shear effects at cavity leading edge is stronger. Our experimental results of the PDF shape and its positive skewness distribution inside the attached cavitation are in accordance with this shear effect theory. Therefore, based on the observations and comparisons with the reported data, it is supposed that the compressibility effects and shear effects are the two main factors influencing the positively skewed PDF shape and its distribution inside the mean attached cavity in our results. Considering that the statistics of pressure fluctuations including r.m.s., Sk, and Ku as a function of ξ/L_c collapse well with σ and are independent on cavity regimes where the bubbly contents inside cavitation changes significantly from inception cavitation to fully developed unsteady cloud cavitation, thus the compressibility, and mainly rely on ξ/L_c , the effects of compressibility on the distribution of the statistics of pressure fluctuations inside the cavity from cavity leading edge to the rear part could be limited. To gain further insight on the statistics of pressure fluctuations, further sophisticated experiment measurement and high-fidelity simulations (e.g., void fractions, sonic speed, and Mach number) are suggested to be conducted to provide detailed information and evidence.

E. Spectral features of wall-pressure fluctuations

In this section, we analyze the spectral features of wall-pressure fluctuations to provide more details about cavitation-induced wall-pressure fluctuations. The Fourier spectra of noise-cancellation wall-pressure fluctuation signals obtained at several streamwise locations inside the mean attached cavity are displayed in Fig. 17. The data sets used in Fig. 17 correspond to the flow conditions in Fig. 13, as listed in Table III, covering a wide range of cavity regimes from stable sheet cavitation to unsteady cloud cavitation, and these data will be used to study the scaling behavior of the various spectral regions of the wall-pressure fluctuation field. The power spectral density function is nondimensionalized using the standard variation of pressure fluctuations (σ_p^2) and the frequency by the cavity length (L_c) and the mean velocity at the wedge throat (U_t) in the following form:

$$\frac{\Phi_p(f)}{\sigma_p^2} \text{ vs } \frac{fL_c}{U_t}. \quad (9)$$

As described in both Figs. 17(a) and 17(b), based on the scaling behaviors of the power spectral density (PSD), four separate spectral regions are distinguished, including the low-frequency ($< 0.3fL_c/U_t$), mid-frequency ($0.3 < fL_c/U_t < 10$), transition-frequency ($10 < fL_c/U_t < 30$), and high-frequency ($30 < fL_c/U_t$) regions. Specifically, the transition-frequency region refers to the connecting region between the mid- and high-frequency regions. In the very low-frequency region below approximately $0.3fL_c/U_t$, a high wall-pressure fluctuation intensity is observed. Within the frequency range ($fL_c/U_t < 0.05$), a constant high PSD value exists, while within the frequency range ($0.05 < fL_c/U_t < 0.3$), fluctuations in the PSD value with frequency can be observed. The PSDs arrive at a local maximum at approximately $0.2fL_c/U_t$, and then the PSD value begins to decrease. This local maximum is the boundary between the low-frequency and mid-frequency regions. In the midfrequency region ($0.3 < fL_c/U_t < 10$), the PSD value decays at an almost constant rate, as observed in Fig. 17(a). Then the PSD value reaches a narrow transition region, after which the decay rate increases suddenly at approximately $30fL_c/U_t$, and this transition region is referred to as the transition region that connects the mid-frequency and high-frequency regions. In the high-frequency region ($fL_c/U_t > 30$), with increasing frequency, the PSD value decreases at a constant decay rate larger than that in the mid-frequency region, as shown in the enlarged figures in Figs. 17(a) and 17(b).

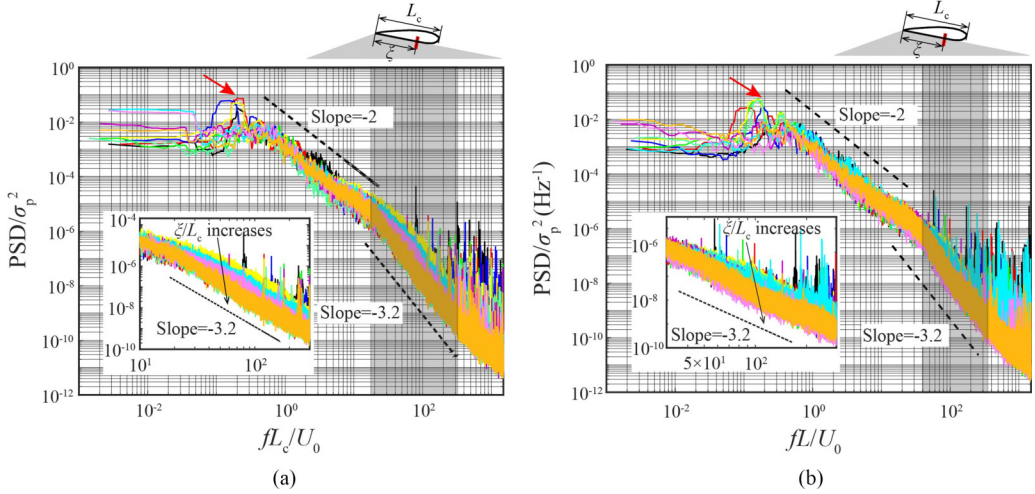


FIG. 17. Distributions of the wall-pressure fluctuation frequency spectrum scaled by cavity length (L_c), mean velocity at wedge throat (U_t) and the standard variation of pressure fluctuations (σ_p^2) inside the mean attached cavity for (a) $Re = 7.8 \times 10^5$ and (b) $Re = 9.5 \times 10^5$. The flow conditions of these data sets are the same as those in Fig. 13, as listed in Table III.

In the following, the scaling behaviors at mid- and high-frequency regions at different streamwise locations are examined. At Reynolds number $Re = 7.8 \times 10^5$, a local maximum $St(= fL_c/U_t)$ is observed at approximately 0.2, as indicated by the red arrows. In the mid-frequency region ($0.2 < fL_c/U_t < 10$), good collapse is observed in PSDs among different streamwise locations, a -2 exponential law is observed, and this scaling is independent of the distance from the cavity leading edge. In the high-frequency region ($fL_c/U_t > 30$), collapse in PSDs among different streamwise locations is no longer observed, and the PSD values decrease with increasing distance from the cavity leading edge, while the scaling law remains the same. From the cavity leading edge to cavity closure, the decay rate changes from a -2 exponential law to a -3.2 exponential law, as displayed in Fig. 17(a). In the transition-frequency region, the decay rate changes from a -2 exponential law to a -3.2 exponential law and experiences the classical $-7/3$ law in a narrow region ($10 < fL_c/U_t < 30$). With the increase in the Reynolds number, the mid-frequency region

TABLE III. Experimental conditions used in Fig. 17.

Line	$Re = 7.8 \times 10^5$			$Re = 9.5 \times 10^5$		
	ξ/L_c	σ	Cavity regime	ξ/L_c	Σ	Cavity regime
—	0.09	0.79	Cloud-RJ	0.10	0.83	Cloud-RJ
—	0.21	0.75	Cloud-RJ	0.21	0.79	Cloud-RJ
—	0.31	0.69	Cloud-RJ	0.31	0.79	Cloud-RJ
—	0.42	0.85	SFS	0.42	0.75	Cloud-SW
—	0.51	0.75	Cloud-RJ	0.52	0.73	Cloud-SW
—	0.60	0.88	SFS	0.64	0.79	Cloud-RJ
—	0.72	0.85	SFS	0.74	0.84	SFS
—	0.80	0.79	Cloud-RJ	0.81	0.80	SFS
—	0.90	0.79	Cloud-RJ	0.92	0.90	SFS
—	1.02	0.85	SFS	1.04	0.85	SFS

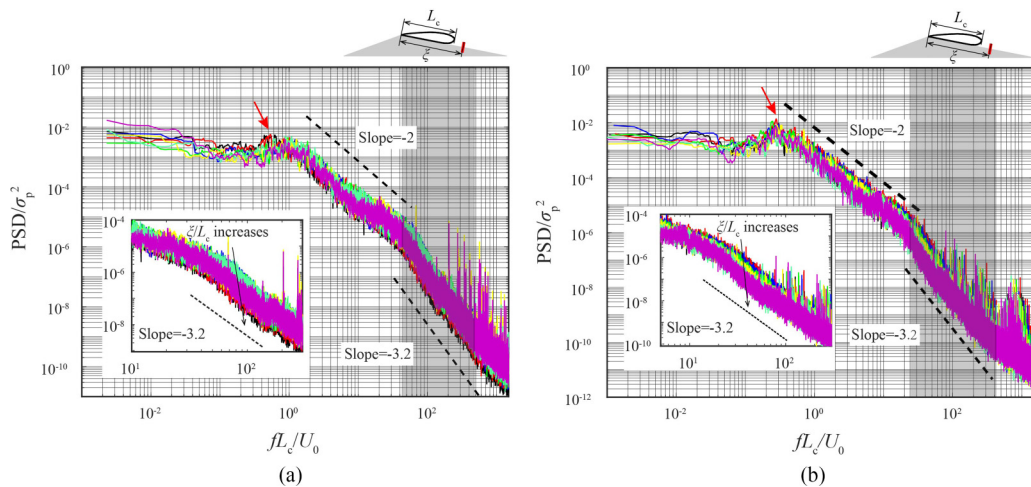


FIG. 18. Distributions of the wall-pressure fluctuation frequency spectrum scaled by cavity length (L_c), mean velocity at wedge throat (U_t) and the standard variation of pressure fluctuations (σ_p^2) outside the mean attached cavity for (a) $\text{Re} = 7.8 \times 10^5$ and (b) $\text{Re} = 9.5 \times 10^5$. The flow conditions of these data sets are the same as those in Fig. 14, as listed in Table IV.

enlarges as the transition frequency between the mid-frequency region and high-frequency region increases, as shown by the shadow region in Fig. 17(b).

To further examine the spectral features of wall-pressure fluctuations outside the mean attached cavity, Fig. 18 shows the frequency spectra at several locations downstream of the mean attached cavity for $\text{Re} = 7.8 \times 10^5$ and $\text{Re} = 9.5 \times 10^5$. The data sets used in Figs. 18 are listed in Table IV. The wall-pressure fluctuation spectra are characterized by four distinct frequency regions, including the low-frequency, mid-frequency, transition-frequency, and high-frequency regions. Similar scaling behaviors at different frequency regions outside the mean attached cavity are seen with those inside the mean attached cavity in Fig. 17, while the major difference falls into the frequency range of the mid-frequency region and the transition point between the low-frequency region and mid-frequency region. As shown in Fig. 18(a), at $\text{Re} = 7.8 \times 10^5$, the mid-frequency region following the -2 scaling law is in the frequency range of $0.5 < fL_c/U_t < 50$ and larger than that inside the mean attached cavity. With the increase in the Reynolds number at $\text{Re} = 9.5 \times 10^5$, the frequency at the transition point decreases, as indicated by red arrows, and the mid-frequency enlarges to the range of $0.3 < fL_c/U_t < 50$, indicating the Reynolds number effects on the mid-frequency contents of wall-pressure fluctuations.

TABLE IV. Experimental conditions used in Fig. 18.

Line	$\text{Re} = 7.8 \times 10^5$			$\text{Re} = 9.5 \times 10^5$		
	ξ/L_c	σ	Cavity regime	ξ/L_c	σ	Cavity regime
—	1.13	0.92	SFS	1.13	0.97	SFS
—	1.40	0.94	SFS	1.30	0.97	SFS
—	1.71	1.08	SIS	1.36	0.90	SFS
—	1.79	1.05	SFS	1.47	0.89	SFS
—	1.87	1.08	SIS	1.62	0.96	SFS
—	2.12	1.07	SIS	1.75	0.97	SFS
—	2.45	0.99	SFS	1.89	1.00	SIS

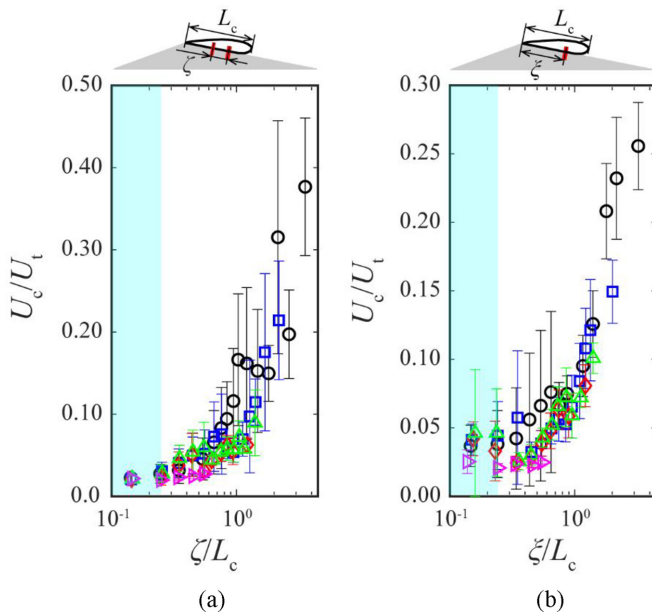


FIG. 19. Evolution of the normalized convection velocity (U_c/U_t) as a function of (a) ζ and (b) ξ/L_c from the most upstream pressure transducer for different cavity regimes under different Re: \circ , $\text{Re} = 7.8 \times 10^5$; \square , 8.7×10^5 ; \diamond , 9.5×10^5 ; \triangle , 1.05×10^6 ; and \blacktriangleright , 1.15×10^6 . The data points from all four pressure transducers under different cavity regimes are collected together, and their means and standard values (error bars) are calculated approximately every $0.1 \xi/L_c$ or $0.1 \zeta/L_c$.

F. Convective velocity distribution in cavitating flows

Further insight into the spectral features of wall-pressure fluctuations can be obtained by examining the convection velocities of the pressure fluctuations. Figure 19 presents the evolution of the convective velocity (U_c) as a function of the spacing (ζ) between the two transducers and the distance of the most upstream transducers from the cavity leading edge (ξ), respectively. The U_c is calculated based on the cross-correlation of pressure fluctuations at two points. In Fig. 19(a), we find that with increasing ζ , U_c increases. Specifically, when $\zeta < L_c$, U_c is approximately 0.00–0.10 U_t , while $\zeta > L_c$, U_c is almost 0.10–0.50 U_t , indicating smaller flow structures within the mean attached cavity compared with that outside the cavity. This is in agreement with the published measurement that the velocity inside the attached cavitation is much lower. Moreover, the data under different Re collapse together, showing the weak Reynolds number effects on U_c inside the attached cavitation. The evolution of U_c as a function of the distance from the most upstream pressure transducer (ξ) shows a similar evolution trend as that as a function of the spacing between transducers (ζ). These results also show the inhomogeneity inside the attached cavitation. The relatively smaller value in Fig. 19(b) could be due to the average processing where the data with different ζ are smoothed. A large ζ favors large-scale structures of the outer flow region, while the pressure transducer data with a small ζ reflect the behavior of the small-scale structures found inside the mean attached cavity. The different values of U_c could be caused by the different flow structures inside and outside the mean attached cavity.

Based on the convective velocity distribution both inside and outside the mean attached cavity in Fig. 19 it can be found that with increasing ξ/L_c , the size of the flow structures increases, while near the cavity leading edge around $\xi/L_c < 0.25$, as indicated by the shadow region, the convective velocity is almost constant, indicating that the size of the flow structures does not change considerably. Combined with the observation of the high-order moments (e.g., S_k and K_u)

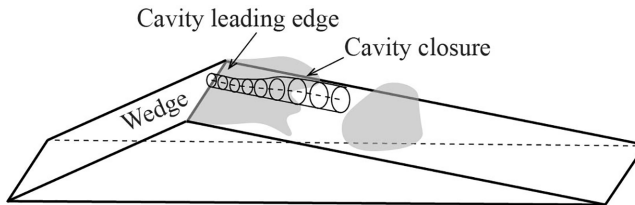


FIG. 20. Sketch of the flow structures in attached turbulent cavitating flows.

distribution of wall-pressure fluctuations in Fig. 15, it can be found that in this region ($\xi/L_c < 0.25$), both Sk and Ku are almost constant. Based on these findings, we illustrate the flow structures in attached cavitating flows in Fig. 20. The flow structures near the cavity leading edge remain almost constant at $\xi/L_c < 0.25$, and then with increasing ξ/L_c , the size of these structures increases gradually. The current work provides information about the flow structure distribution in cavitating flows. However, considering that cavitation bubble dynamics are essential to the characteristics of wall-pressure fluctuations, further work can be conducted to include the details of cavitation bubble dynamics in the analysis of wall-pressure fluctuations induced by cavity behaviors.

IV. SUMMARY AND DISCUSSION

In this study, we provide an experimental investigation of the characteristics and physics of wall-pressure fluctuations beneath attached turbulent cavitation, especially on the statistics and their scaling behaviors. Experiments were conducted in a high-speed water tunnel with a convergent-divergent wedge test model. Unstable turbulent cavitating flows were generated in the separated region of the 10° divergent section of a backward-facing wedge model with varying cavitation numbers under five fixed Reynolds number conditions. Observations of transient cavity behaviors were acquired with high-speed imaging, and the wall-pressure fluctuations were measured by flush-mounted dynamic pressure transducers. A simultaneous sampling technique was employed to synchronize the wall-pressure fluctuation measurement with high-speed imaging. Multipoint pressure measurements with an array of four high-frequency unsteady PCB transducers in the streamwise direction along the wall surface provided a data set of the cavitation-induced wall-pressure fluctuation signals both inside and outside the mean attached cavity.

The principal findings from this study are as follows:

(1) Our study shows that the mean cavity structures under different cavity regimes show geometrical similarity, and thus, a normalized scaling parameter is correspondingly proposed. The observation of transient cavity behaviors shows that four distinct cavitation regimes are observed in the current experiment, including relatively stable inception cavitation (SIS), stable sheet cavitation (SFS), and unsteady quasiperiodic cloud cavitation (cloud cavitation-RJ and cloud cavitation-SW). However, the mean cavity structures, especially the geometric shapes, show self-similarity. Quantitative analysis of the mean geometry metrics, including L_c , L_{tc} , t_c , and θ , elucidates that with decreasing σ , the cavitation region expands explosively, and the mean cavity length (L_c and L_{tc}) and maximum mean cavity thickness (t_c) increase as a negative exponent of approximately -5.0 . The mean slenderness factor (θ) shows the trend of first increasing and then decreasing, which means that the cavity content expands mainly vertically first and then in the streamwise direction. A larger θ shows stronger cavity/liquid impingement across the cavity interface. Inspired by this geometric self-similarity in terms of mean cavity structures under different cavity regimes, we proposed the parameter ξ/L_c , i.e., the normalized distance from the cavity leading edge, to identify the position inside and outside the mean cavity. Remarkably, several statistical features of wall-pressure fluctuations in cavitating flow fields independent of cavitation regimes both inside and outside the mean cavity region are revealed by scaling with ξ/L_c .

(2) The root mean square (r.m.s.), probability density function (PDF), high-order moments (Sk, Ku), and convection velocity (U_c) of cavitation-induced wall-pressure fluctuations are primarily dependent on the distance from the cavity leading edge (ξ/L_c) but independent of the cavity regimes (i.e., inception, sheet, and cloud cavity). Apart from the classical high wall-pressure fluctuation intensity at the transient cavity closure for stable sheet cavity regimes reported in the literature, the study has revealed several statistics of pressure fluctuation distribution occurring from the mean cavity leading edge to the mean cavity closure under different flow regimes, including stable inception and sheet cavity and unsteady cloud cavity. Specifically, according to ξ/L_c , we combine the data under different cavity regimes and Reynolds numbers and find that with the increase in ξ/L_c , inside the mean attached cavitation, the r.m.s. of the wall-pressure fluctuation coefficient increases and arrives at its maximum near the mean cavity closure. Outside the mean attached cavity, the r.m.s. of wall-pressure fluctuations attenuates with increasing ξ/L_c at an attenuation rate smaller than the enhancement rate of wall-pressure fluctuations r.m.s. inside the mean attached cavity. It is worth noting that although the unsteadiness of flow structures at cavity closure is totally different (i.e., relatively stable inception cavity closure, small-scale shedding sheet cavity closure and large-scale shedding cloud cavity closure), this phenomenon is independent of σ (thus, cavity regimes) as long as it scales with ξ/L_c . In addition, with increasing Re, the r.m.s. coefficient increases, indicating that although the mean cavity shape is the same, the wall-pressure fluctuation intensity at high Re could be larger and have much more potential damage. We also examine the statics of wall-pressure fluctuations. First, the PDF inside the attached cavitation shows non-Gaussian and asymmetrical characteristics both inside and outside the cavity, while near cavity closure, it shows Gaussian and symmetric characteristics. The PDF shape inside the attached cavitation is positively skewed and dependent on ξ/L_c , while that outside the mean attached cavity is slightly negatively skewed. By calculating the high-order moments (Sk and Ku), the non-Gaussian character of wall-pressure fluctuations in cavitating flows is quantitatively confirmed, where inside the mean attached cavity ($\xi/L_c < 1$), $Sk > 0$, $Ku > 3$, and outside the mean attached cavity ($\xi/L_c > 1$), $Sk < 0$, $Ku > 3$. Across the cavity closure in the far fields downstream of the cavity, both Sk and Ku approach constant values with $Sk < 0$ and $Ku > 3$, showing non-Gaussian behaviors that are slightly negatively skewed and almost independent of ξ/L_c . Furthermore, this non-Gaussian and asymmetric behavior shows Reynolds number dependence, and with increasing Re, it is enhanced. Finally, we propose the hypothesis that the compressibility effects and shear effects contribute to this positively skewed PDF shape and its distribution inside the attached cavitation, and considering the cavitation bubble dynamics, the compressibility effects play a dominant role rather than the shear effects.

(3) To study the scaling behaviors of wall-pressure fluctuations in cavitating flows, we investigate the spectral characteristics. The spectral analysis obtained by fast Fourier transform (FFT) shows that based on the scaling behaviors, four distinct frequency regions, i.e., low-frequency, mid-frequency, transition-frequency, and high-frequency regions, are identified. The mid-frequency and high-frequency regions follow the -2 and -3.2 laws, respectively. The $-7/3$ scaling law is also observed in the transition-frequency region. In the high-frequency regions, with the increase in ξ/L_c , i.e., from the cavity leading edge to cavity closure, the scaling behavior remains the same while the wall-pressure fluctuation intensity level decreases. To provide insights into the internal flows of the mean attached cavity, the distribution of convective velocity is calculated. We find that with the increase in both the spacing between the pressure transducers ζ/L_c and the distance from the cavity leading edge of the most upstream pressure transducers ξ/L_c , the convective velocity increases. Specifically, inside the mean attached cavity ($\xi/L_c < 1$), the normalized convective velocity is in the range of below $0.1 U_t$ and outside mean attached cavity ($\xi/L_c > 1$) $0.1-0.5 U_t$, indicating the small cavitation flow structures inside the attached cavitation compared with those outside the mean attached cavity.

Finally, we would like to note a number of limitations of our current measurements; the corresponding caution needs to be taken about our results as well as the suggestions for future investigation.

Our study has demonstrated several features of cavitation-induced wall-pressure fluctuations from a statistical viewpoint. The maximum wall-pressure fluctuation intensity level is located near the cavity closure region of the mean cavitating flow fields, which indicates that the pressure load is strong there. Moreover, the PDFs of wall-pressure fluctuations present non-Gaussian behaviors both inside and outside the mean cavity, which could induce different pressure loads compared with those following the Gaussian distribution. It is known that the pressure load following a Gaussian process is different from that following a non-Gaussian process. Thus, to improve the prediction accuracy of pressure loads on solid materials, it is suggested to include both the root mean square value and high-order moments (e.g., skewness and kurtosis) of wall-pressure fluctuations to establish a new criterion for the evaluation of load and thus cavitation erosion. This study could provide information about the pressure load distribution and its characteristics in cavitating flow fields and help the optimization of hydraulic designs. According to our results, from the cavity leading edge to cavity closure inside the mean attached cavity, the frequency spectral strength in the high-frequency region of wall-pressure fluctuations decreases, showing the flow structures associated with high-frequency attenuation. In combination with the convection velocity distribution inside the mean attached cavity, we find that the scales of flow structures increase from the cavity leading edge to cavity closure.

The present study is able to provide comprehensive knowledge of the characteristics of wall-pressure fluctuations in turbulent cavitating flows, which can provide information on internal flows inside a mean attached cavity. Such information is critical for understanding both the fundamental turbulence structures in turbulent cavitating flows and provides data to solve problems of practical interest, e.g., sources of noise and vibrations, which is a primary concern when vehicles are operated in cavitation conditions and has not been well understood. We note that in single separated and reattachment flows, the large-scale structures in the shear layer and the flapping motion (low frequency) at the separation region are important sources in the generation of wall-pressure fluctuations rather than the near wall behaviors bounded in the recirculation region [40]. This provides an interesting viewpoint of wall-pressure fluctuations inside cavitation, especially the flow regimes in the current study (SIS, SFS, cloud cavitation-RJ, which mainly interacts with the recirculation region, and cloud cavitation-SW, which interacts with both the shear layer and recirculation region in single phase flows). Owing to the interactions between the multiphase flow and turbulence in cavitating flows, the generation mechanisms of wall-pressure fluctuations inside the cavitation region are much more complex than those in single-phase turbulent separated and reattachment flows. Further study is required to improve the understanding of the role of the cavitation shear layer, reentrant jet and shockwave and their interactions with local turbulent structures in cavitation-induced wall-pressure fluctuations. Some mechanisms of the flow structures (e.g., cavitation shear layer, reentrant, and shockwave) and their correlation with wall-pressure fluctuations are to be deepened, particularly in the frequency and spectral space. Further studies could be conducted to investigate in detail the synergy mechanism of compressibility and shear effects on the PDF shape and its distribution of the wall-pressure fluctuations inside the attached cavitation.

This work provides additional knowledge on the statistics and source of wall-pressure fluctuations inside attached cavitation behind a 10° divergent channel in the test section of a high-speed water tunnel and can be used as a guide for cavitation model improvement in numerical simulations. In state-of-art cavitation modeling, especially transport-based cavitation models, only the local static pressure (p) is adopted to calculate the phase change rate between liquid and vapor, while no information about the pressure fluctuations (p') is included. Our study shows that the pressure fluctuations inside attached cavitation present nonuniform and unique characteristics from the cavity leading edge to cavity closure. Our study suggests the use of $(p + p')$ instead of (p) in the cavitation model. Previous work has modeled the effects of p' on local saturated pressure based on fluctuating velocity fields [51], and our study further provides quantitative estimation of p' using fluctuating pressure fields. Furthermore, considering the non-Gaussian behaviors of wall-pressure fluctuations in cavitating flows, to better predict the cavitation loads on solid material and thus cavitation erosion, it is suggested to establish a criterion that includes both the r.m.s. value and Sk of wall-pressure

fluctuation, rather than only the r.m.s. value. In future work, this unique characteristic, which is dependent on the distance from the cavity leading edge (ξ/L_c), could be further simplified and modeled and provide information about the fluctuating pressures to improve the cavitation modeling accuracy.

ACKNOWLEDGMENTS

Financial support by grants from the National Natural Science Foundation of China (51839001, 52079004, 51979003, U20B2004) is gratefully acknowledged. C.W. is grateful for the financial support of the China Scholarship Council (CSC, Grant No. 201906030144) for her visit at Saint Anthony Falls Laboratory of the University of Minnesota and the Hong Kong Polytechnic University Postdoc Matching Fund Scheme (Grant No. 1-W245).

-
- [1] X. Liu and J. Katz, Cavitation phenomena occurring due to interaction of shear layer vortices with the trailing corner of a two-dimensional open cavity, *Phys. Fluids* **20**, 041702 (2008).
 - [2] G. K. Batchelor, *An Introduction to Fluid Dynamics* (Cambridge University Press, New York, 1967).
 - [3] C. E. Brennen, *Cavitation and Bubble Dynamics* (Oxford University Press, Oxford, 1995).
 - [4] D. D. Joseph, Cavitation in a flowing liquid, *Phys. Rev. E* **51**, R1649(R) (1995).
 - [5] A. Amini, J. Seo, S. H. Rhee, and M. Farhat, Mitigating tip vortex cavitation by a flexible trailing thread, *Phys. Fluids* **31**, 127103 (2019).
 - [6] E. Kadivar, M. V. Timoshevskiy, M. Y. Nichik, M. Y. Nichik, O. el Moctar, T. E. Schellin, and K. S. Pervunin, Control of unsteady partial cavitation and cloud cavitation in marine engineering and hydraulic systems, *Phys. Fluids* **32**, 052108 (2020).
 - [7] W. Liu, Ning Li, C. Weng, X. Huang, and Y. Kang, Bubble dynamics and pressure field characteristics of underwater detonation gas jet generated by a detonation tube, *Phys. Fluids* **33**, 023302 (2021).
 - [8] H. Cheng, X. Long, B. Ji, X. Peng, and M. Farhat, Suppressing tip-leakage vortex cavitation by overhanging grooves, *Exp. Fluids* **61**, 159 (2020).
 - [9] M. Brunhart, C. Soteriou, M. Gavaises, M. Gavaises, I. Karathanassis, P. Koukouvinis, S. Jahangir, and C. Poelma, Investigation of cavitation and vapor shedding mechanisms in a Venturi nozzle, *Phys. Fluids* **32**, 083306 (2020).
 - [10] M. A. Maiga, O. Coutier-Delgosha, and D. Buisine, Analysis of sheet cavitation with bubble/bubble interaction models, *Phys. Fluids* **31**, 073302 (2019).
 - [11] Y. Saito, R. Takami, I. Nakamori, and T. Ikhagi, Numerical analysis of unsteady behavior of cloud cavitation around a NACA0015 foil, *Comput. Mech.* **40**, 85 (2007).
 - [12] P. J. Zwart, A. G. Gerber, and T. Belamri, A two-phase flow model for predicting cavitation dynamics, in *Proceedings of ICMF-2004 the Fifth International Conference on Multiphase Flow*, edited by Y. Matsumoto, K. Hishida, A. Tomiyama, K. Mishima, and S. Hosokawa in cooperation with the members of the International Scientific Committee (Yokohama, Japan, 2004), p. 152.
 - [13] K. R. Laberteaux and S. L. Ceccio, Partial cavity flows. Part 2: Cavities forming on test objects with spanwise variation, *J. Fluid Mech.* **431**, 43 (2001).
 - [14] H. Ganesh, S. A. Mäkiharju, and S. L. Ceccio, Bubbly shock propagation as a mechanism for sheet-to-cloud transition of partial cavities, *J. Fluid Mech.* **802**, 37 (2016).
 - [15] H. Rouse and J. S. McNown, *Cavitation and Pressure Distribution: Head Forms at Zero Angle of Yaw* (State University of Iowa, Iowa, 1948).
 - [16] Y. Shen and P. E. Dimotakis, The influence of surface cavitation on hydrodynamic forces, in *Proceedings of 22nd American Towing Tank Conference* (St. John's, Newfoundland, Canada, 1989), pp. 44–53.
 - [17] Q. Le, J. P. Franc, and J. M. Michel, Partial cavities: Global behavior and mean pressure distribution, *J. Fluid Eng.* **115**, 243 (1993).

- [18] K. K. Ooi and A. J. Acosta, The utilization of specially tailored air bubbles as static pressure sensors in a jet, *J. Fluid Eng.* **106**, 459 (1984).
- [19] T. J. O'Hern, An experimental investigation of turbulent shear flow cavitation, *J. Fluid Mech.* **215**, 365 (1990).
- [20] B. Ran and J. Katz, The response of microscopic bubbles to sudden changes in the ambient pressure, *J. Fluid Mech.* **224**, 91 (1991).
- [21] B. Ran and J. Katz, Pressure fluctuations and their effect on cavitation inception within water jets, *J. Fluid Mech.* **262**, 223 (1994).
- [22] A. L. Porta, G. A. Voth, F. Moisy, and E. Bodenschatz, Using cavitation to measure statistics of low-pressure events in large-Reynolds-number turbulence, *Phys. Fluids* **12**, 1485 (2000).
- [23] M. Bappy, P. M. Carrica, and G. C. Buscaglia, Lagrangian statistics of pressure fluctuation events in homogeneous isotropic turbulence, *Phys. Fluids* **31**, 08511 (2019).
- [24] M. Bappy, P. M. Carrica, A. Vela-Martín, A. Vela-Martín, L. S. Freire, and G. C. Buscaglia, Pressure statistics of gas nuclei in homogeneous isotropic turbulence with an application to cavitation inception, *Phys. Fluids* **32**, 095107 (2020).
- [25] G. Bark and W. B. Berlekomp, Experimental investigations of cavitation noise, in *Proceedings of the 12th ONR Symposium on Naval Hydrodynamics* (National Academy of Sciences, Washington, D C, 1978), pp. 470–493.
- [26] G. Bark, Developments of distortions in sheet cavitation on hydrofoils, in *Proceedings of the ASME International Symposium on Jets and Cavities* (ASME, New York, 1985), pp. 470–493.
- [27] J. Wu, H. Ganesh, and S. Ceccio, Multimodal partial cavity shedding on a two-dimensional hydrofoil and its relation to the pressure of bubbly shocks, *Exp. Fluids* **60**, 66 (2019).
- [28] C. Esposito, M. A. Mendez, J. Steelant, and M. R. Vetrano, Spectral and modal analysis of a cavitating flow through an orifice, *Exp. Therm. Fluid Sci.* **121**, 110251 (2020).
- [29] Q. Le, J. P. Franc, and J. M. Michel, Partial cavities: Pressure pulse distribution around cavity closure, *J. Fluid Engng.* **115**, 249 (1993b).
- [30] G. E. Reisman, Y. C. Wang, and C. E. Brennen, Observations of shock waves in cloud cavitation, *J. Fluid Mech.* **355**, 255 (1998).
- [31] J. B. Leroux, J. A. Astolfi, and J. Y. Billard, An experimental study of unsteady partial cavitation, *J. Fluids Eng.* **126**, 94 (2004).
- [32] G. Chen, G. Wang, C. Hu, B. Huang, and M. Zhang, Observations and measurements on unsteady cavitating flows using a simultaneous sampling approach, *Exp. Fluids* **56**, 32 (2015).
- [33] C. Wang, B. Huang, G. Wang, M. Zhang, and N. Ding, Unsteady pressure fluctuation characteristics in the process of breakup and shedding of sheet/cloud cavitation, *Int. J. Heat Mass Transfer* **114**, 769 (2017).
- [34] X. Li, G. Wang, M. Zhang, and W. Shyy, Structures of supercavitating multiphase flows, *Int. J. Therm. Sci.* **47**, 1263 (2008).
- [35] M. K. Bull, Wall-pressure fluctuations associated with subsonic turbulent boundary layer flow, *J. Fluid Mech.* **28**, 719 (1967).
- [36] R. T. Knapp, Recent investigations of the mechanics of cavitations and cavitation damage, *Trans. ASME* **77**, 1045 (1955).
- [37] Y. Kawanami, H. Kato, H. Yamaguchi, M. Tanimura, and Y. Tagaya, Mechanism and control of cloud cavitation, *J. Fluids Eng.* **119**, 788 (1997).
- [38] M. Callenaere, J. P. Franc, J. M. Michel, and M. Riondet, The cavitation instability induced by the development of a re-entrant jet, *J. Fluid Mech.* **444**, 223 (2001).
- [39] O. Coutier-Delgosha, B. Stutz, A. Vabre, and S. Legoupil, Analysis of cavitating flow structure by experimental and numerical investigations, *J. Fluid Mech.* **578**, 171 (2007).
- [40] W. J. Devenport and E. P. Sutton, Near-wall behavior of separated and reattaching flows, *AIAA J.* **29**, 25 (1991).

- [41] P. A. Lush and P. I. Peters, Visualization of the cavitating flow in a venturi type duct using high speed cinephotography, in *Proceedings of the Conference on Operating Problems of Pump Stations and Power Plants, International Association for Hydraulic Research (IAHR)* (Amsterdam, The Netherlands, 1982), p. 5.
- [42] B. Stutz and J. L. Reboud, Experiments on unsteady cavitation, *Exp. Fluids* **22**, 191 (1997).
- [43] M. Dular, I. Khelifa, S. Fuzier, M. Adama Maiga, and O. Coutier-Delgosha, Scale effect on unsteady cloud cavitation, *Exp. Fluids* **53**, 1233 (2012).
- [44] R. Camussi, M. Felli, F. Pereira, G. Aloisio, and A. Di Marco, Statistics properties of wall pressure fluctuations over a forward-facing step, *Phys. Fluids* **20**, 075113 (2008).
- [45] A. Pumir, A numerical study of pressure-fluctuations in three-dimensional, incompressible, homogeneous, isotropic turbulence, *Phys. Fluids* **6**, 2071 (1994).
- [46] Y. Tsuji, J. H. M. Fransson, P. H. Alfredsson, and A. V. Johansson, Pressure statistics and their scaling in high-Reynolds-number turbulent boundary layers, *J. Fluid Mech.* **585**, 1 (2007).
- [47] D. A. Donzis and S. Jagannathan, Fluctuations of thermodynamic variables in stationary compressible turbulence, *J. Fluid Mech.* **733**, 221 (2013).
- [48] J. P. Franc and J. M. Michel, *Fundamentals of Cavitation* (Kluwer Academic Publishers, New York, Boston, Dordrecht, London, Moscow, 2004).
- [49] S. B. Pope, *Turbulent Flows* (Cambridge University Press, Cambridge, 2000).
- [50] W. K. Blake, Complex flow-structure interactions, *Mechanics of Flow-Induced Sound and Vibration*, 2nd ed., Vol. 2: Complex Flow-Structure Interactions (Elsevier Academic Press, Orlando, FL, 2017).
- [51] A. K. Singhal, M. M. Athavale, H. Y. Li, and Y. Jiang, Mathematical basis and validation of the full cavitation model, *J. Fluid. Eng.* **124**, 617 (2002).